



## RESEARCH ACTIVITIES

### Materials Molecular Science

Extensive developments of new molecules, molecular systems and their higher-order assemblies are being conducted in three Divisions of Electronic Structures, Electronic Properties, and Molecular Functions, one division for visiting professors, and Research Center for Molecular Scale Nanoscience, in an attempt to discover new phenomena and useful functions. The physical properties of electronic, optical and magnetic properties on new functional materials are investigated, and moreover, the chemical properties like catalysis and photochemistry and technological applications like solar cells are also examined in this department.

# Graphene-Walled Alveolate Carbon & Structures and Functions of Metal–Carbon Nano-Systems Made from Metal-Acetylides

Department of Materials Molecular Science  
Division of Electronic Structure



NISHI, Nobuyuki  
JUDAI, Ken  
NISHIJO, Junichi  
USUI, Chika

Professor\*  
Assistant Professor†  
Assistant Professor  
Technical Fellow & Secretary

Metal acetylides or metal ethynyl molecules are made of the  $M^+-C^-$  ionic bonds. However, the ionic states of the acetylides are essentially metastable resulting in the segregation into metal-carbon or metal-organic polymer nanophases. Following to the invention of graphene-singlewalled Mesoporous Carbon Nano Dendrites (MCND) by evaporating silver from dendroid silver acetylide crystals, we have invented Graphene-multiwalled Alveolate Carbon (GAC), this time, and also 3D nanonets with GAC. These highly electron-conductive materials can be used for the electrodes of various next generation batteries.

## 1. Improvement of Graphene-Multiwalled Alveolate Carbon for Novel Battery Electrodes

As demonstrated by many researchers, graphene single sheets and multiple layers are successfully prepared on the ultra-clean surface of metallic copper, nickel or iron. Chemical vapor deposition (CVD) of acetylene or methane produces  $C_2$  radicals that forms condensed hexagonal rings (*i.e.* graphene) with  $\pi$ -orbitals sitting on the d- and s- orbitals of the metal surface. This happens on the gas-solid interface at relatively high temperatures. In order to make a graphene walled mesoporous carbon, copper methylacetylide wire crystals are used with coating iron compound layers that prevent the acetylide segregation reaction explosive. Copper nanoparticles are generated and methyl radicals are converted to methane and ethylene leaving  $C_2$  radicals on the surface of copper particles. On the heating of the reactant, copper metals get away from the inner space to outside leaving the quasi-spherical (originally spherical) pores with walls made of two or three graphene layers as shown in figure 1b. As seen in the figure, all carbons in this alveolate

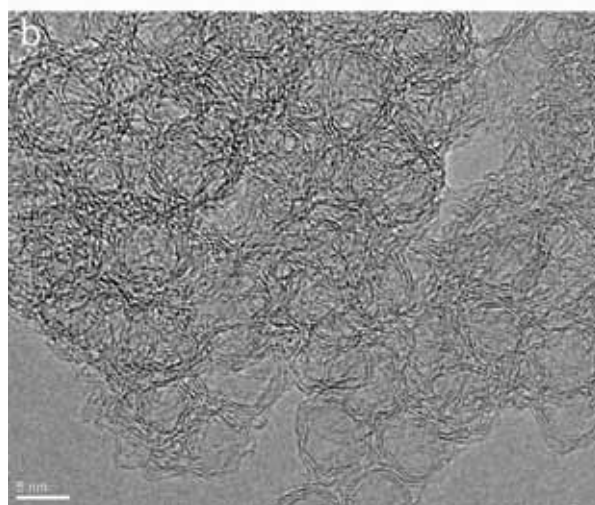
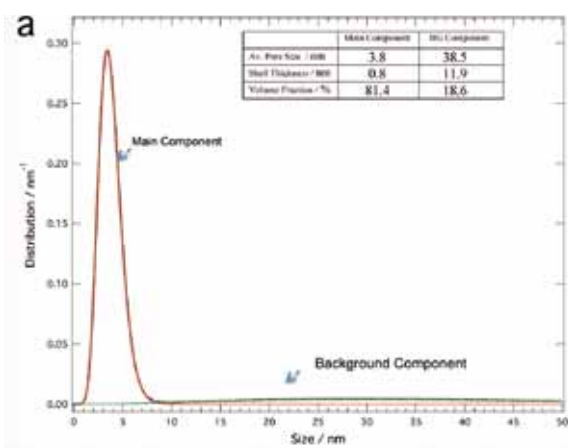


**Figure 1.** a: Core/shell analysis and the pore size distribution of the improved Graphene-multiwalled Alveolate Carbon. b: A TEM image of the improved Graphene-multiwalled Alveolate Carbon.

carbon are graphene sheets. Amorphous carbon is evacuated as CO<sub>2</sub> gas leaving micro- or meso-pores in the body and increasing the BET surface area of the alveolate carbon. Now, use of this carbon is under aggressive examination for various battery electrodes.

## 2. In Situ Preparation and Catalytic Activation Method for Copper Nanoparticles from Acetylide Molecules<sup>1)</sup>

Because metal nanoparticles have a high surface area to volume ratio, they can be highly reactive, cost-effective catalysts. However, metallic surfaces are usually too reactive to maintain their metallic character in the presence of oxygen and/or water vapor. Metal nanoparticle catalysts must be handled carefully to avoid oxidation and inactivation. Here, we suggest a facile in situ preparation method for metal nanoparticle catalysts. Copper acetylide and copper methyl-acetylide molecules are based on ionic bonding, and are relatively stable in air. They can be used as a precursor of copper nanoparticles. Due to their instability at increased temperatures, subsequent annealing promotes a segregation reaction into elemental copper and carbon. Transmission electron microscopy and powder X-ray diffraction revealed that the average diameters of the Cu nanoparticles thus formed were 13.3 and 4.4 nm for C<sub>2</sub>Cu<sub>2</sub> and CuCC-CH<sub>3</sub> precursors, respectively. This suggests that the substitution of acetylide molecules can control the size of the resulting copper nanoparticles. The primary advantage of this preparation method is that the functional acetylide group can reduce copper cations. No additional reducing agent is required, so no further separation process is necessary. This presents in situ preparation process. The catalytic activity of the resulting Cu nanoparticles was confirmed for a hydrogen storage system.

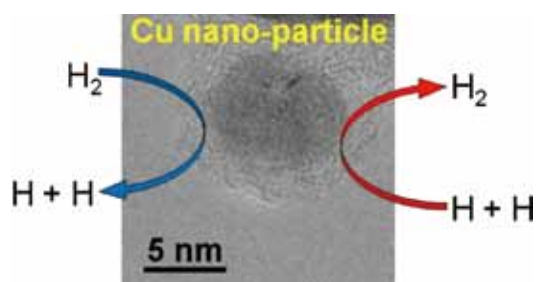
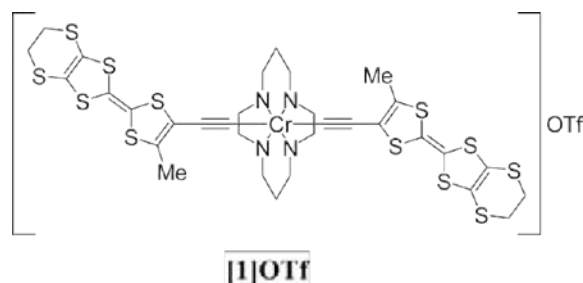


**Figure 2.** Scheme of hydrogen conversion by Cu nanoparticles covered with amorphous carbon mantles.

## 3. Weak Ferromagnetism and Strong Spin-Spin Interaction Mediated by the Mixed-Valence Ethynyltetraathiafulvalene-Type Ligand<sup>2)</sup>

A new chromium complex with ethynyl-tetraathiafulvalene (TTF) type ligands, [CrCyclam(C≡C-5-methyl-4'5'-ethylene-dithio-TTF)<sub>2</sub>OTf] ([1]OTf), was synthesized. The cyclic voltammetry of the complex shows reversible two oxidation waves owing to the first and second oxidation of TTF unit. The electrochemical oxidation of [1]OTf in Bu<sub>4</sub>NClO<sub>4</sub> or Bu<sub>4</sub>NBF<sub>4</sub> solution of acetonitrile-chlorobenzene 1:1 mixture gave isostructural crystals of [1][ClO<sub>4</sub>]<sub>2</sub>(PhCl)<sub>2</sub>(MeCN) and [1][BF<sub>4</sub>]<sub>2</sub>(PhCl)<sub>2</sub>(MeCN), where two mixed-valence TTF units of adjacent complexes form dimer cation radical. The crystal structures are characterized by the alternate chain of  $S = 3/2$  Cr<sup>3+</sup>Cyclam units and  $S = 1/2$  (TTF)<sup>2+</sup> dimers. These two paramagnetic components are connected directly by ethynyl group, resulting in the strong intra-chain spin-spin interaction of  $2J/k_B = -30$  and  $-28$  K for [ClO<sub>4</sub>]<sup>-</sup> and [BF<sub>4</sub>]<sup>-</sup> salts, respectively ( $H = -2J\sum_i S_i S_{i+1}$ ). Both salts show weak-ferromagnetic transition at 23 K thanks to inter-chain anti-ferromagnetic interaction between TTF dimers. The remanent magnetizations and coercive forces of non-oriented samples at 1.8 K are 0.016 μB and 90 mT for the [ClO<sub>4</sub>]<sup>-</sup> salt, and 0.010 μB and 50 mT Oe for the [BF<sub>4</sub>]<sup>-</sup> salt, respectively. The weak-ferromagnetism is attributed to the Dzyaloshinsky-Moriya interaction between adjacent TTF dimers and / or the single ion anisotropy of [1]<sup>2+</sup>.



### References

- 1) K. Judai, S. Numao, J. Nishijo and N. Nishi, *J. Mol. Catal. A: Chem.* **347**, 28–33 (2011).
- 2) J. Nishijo, K. Judai and N. Nishi, *Inorg. Chem.* **50**, 3464–3570 (2011).

\* Present Address; Nagoya Institute of Technology, Tokyo Institute of Technology

† Present Address; College of Humanities and Sciences, Nihon University

# Characterization of Magnetic Ultrathin Films by Novel Spectroscopic Methods

Department of Materials Molecular Science  
Division of Electronic Structure



YOKOYAMA, Toshihiko	Professor
NAKAGAWA, Takeshi	Assistant Professor
TAKAGI, Yasumasa	Assistant Professor
EGUCHI, Keitaro	Graduate Student
FUNAKI, Yumiko	Secretary
IWATA, Yumi	Secretary
KOSHIMIZU, Junko	Secretary

Novel properties of magnetic metal ultrathin films have been attractive both from fundamental interest and from technological requirements. We are especially interested in drastic modification of metal thin films by surface chemical treatment such as adsorption-induced spin transitions and morphological changes. The magnetic properties are characterized by means of several kinds of spectroscopic methods like MOKE (Magneto-Optical Kerr Effect) using UV-visible lasers and XMCD (X-ray Magnetic Circular Dichroism) using synchrotron radiation soft X-rays.

Moreover, we have been exploiting new techniques based on UV photoemission magnetic circular dichroism (MCD) such as ultrafast time resolved UV MCD photoelectron emission microscopy (PEEM) for spatiotemporal magnetic imaging.

## 1. Growth Process and Magnetic Properties of Fe Nanoparticles Deposited on Si<sub>3</sub>N<sub>4</sub>/Si(111)-(8×8)

The magnetic properties of ferromagnetic transition metals on Si substrates have been widely investigated for the exploitation of new magnetic devices. Since clean Si surfaces react with transition metals very easily to form usually non-magnetic transition-metal silicides, it is essential to insert some inert film between transition metals and Si substrate. No reports have been however published for epitaxially ordered substrates on Si(111). In the present study, we investigated growth processes and magnetic properties of Fe deposited on well-defined Si<sub>3</sub>N<sub>4</sub>/Si(111)-(8×8), by using STM and XMCD.

Figures 1(a) and 1(b) show the STM images of the Si<sub>3</sub>N<sub>4</sub>/Si(111)-(8×8) substrate surface and 7.5 ML (monolayer) Fe deposited on the substrate. The substrate surface exhibits clear (8×8) superstructure that was also verified by LEED (low energy electron diffraction). The 7.5 ML Fe film shows the formation of Fe nanoparticles with the average diameter of ~6.9 nm. Figure 1(c) shows the Fe L-edge XMCD spectra of Fe deposited on Si<sub>3</sub>N<sub>4</sub>/Si(111)-(8×8) and clean Si(111)-(7×7). It is clearly found that the XMCD signals of Fe/Si<sub>3</sub>N<sub>4</sub> are

much larger than those of Fe/Si(111), especially for small Fe coverages. Figure 2(d) shows the magnetization curves of 1.6

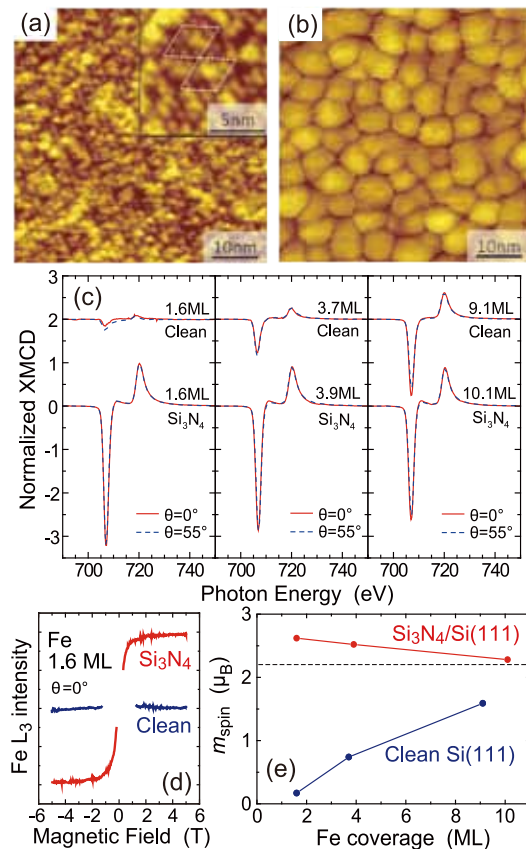


**Figure 1.** (a,b) 55×55nm<sup>2</sup> STM images of (a) Si<sub>3</sub>N<sub>4</sub>/Si(111)-(8×8) substrate and (b) the 7.5 ML Fe deposited film on the substrate. (c) Fe L<sub>3,2</sub>-edge XMCD of Fe on clean Si(111) and Si<sub>3</sub>N<sub>4</sub> at  $\mu_0 H = \pm 5$  T and  $T = 5$  K. The X-ray incidence angles  $\theta$  are 0° (normal incidence) and 55° (grazing). (d) Magnetization curves of 1.6 ML Fe on clean Si(111) (blue) and Si<sub>3</sub>N<sub>4</sub> (red), taken at  $T = 5$  K and  $\theta = 0^\circ$  by fixing the photon energy at the L<sub>3</sub> peak top. (e) Spin magnetic moments  $m_{\text{spin}}$  of Fe on clean Si(111) (blue) and Si<sub>3</sub>N<sub>4</sub> (red) at  $T = 5$  K as a function of Fe coverage.

ML Fe on the two substrates, again exemplifying a large and almost no magnetization of Fe on  $\text{Si}_3\text{N}_4$  and clean Si(111), respectively. The XMCD spectra in Figure 1(c) allow us to obtain spin and orbital magnetic moments by using the so-called sum rules. The results are given in Figure 1(e). On clean Si(111)-(7×7), the spin magnetic moment is very small at low coverage and is enhanced with the increase in Fe coverage. On the contrary, Fe/ $\text{Si}_3\text{N}_4$  has a much larger spin magnetic moment of  $2.62 \mu_B$ , which is even larger than that of bcc bulk Fe ( $2.2 \mu_B$ ). Such a drastic difference between the clean Si and  $\text{Si}_3\text{N}_4$  substrates is caused by the fact that the  $\text{Si}_3\text{N}_4$  substrate effectively suppresses the silicide formation. Because of the weak interaction with the  $\text{Si}_3\text{N}_4$  substrate and the mismatch of the lattice constant, Fe/ $\text{Si}_3\text{N}_4$  grows as nanoparticles that exhibit superparamagnetism. A larger spin magnetic moment at small Fe coverage is attributed to the size effect; the reduction of the particle size enhances the ratio of surface atoms that may exhibit larger magnetic moments.

## 2. Anharmonicity and Quantum Effects in Thermal Expansion of an Invar Alloy<sup>1</sup>

Anomalously small thermal expansion over a wide temperature range in an iron-nickel alloy with a nickel concentration of around 35% was discovered by Guillaume in 1897, who was awarded the Nobel Prize in Physics in 1920. The effect is well known as the Invar effect and has been utilized in various kinds of industrial products. It has been recognized that the effect originates from magnetism. A basic concept of the Invar effect is that there exist at least two types of electronic states in Fe, typically high-spin (HS) and low-spin (LS) states. In this two-state model, the equilibrium potential energy is lower in the HS state than in the LS one, while the equilibrium atomic radius is larger in the former. This results in the compensation of thermal expansion due to increasing density of the LS state at higher temperature. Computational simulations at finite temperatures have also been carried out for the understanding of magnetization and thermal expansion. There have been, however, no reports concerning quantum-mechanical dynamics calculations, such as path-integral Monte Carlo (MC) simulations, although in general thermal expansion inherently results from anharmonic vibration, to which the quantum effect is essentially important at low temperature. In this work, we have investigated the anharmonicity and quantum effects in the Invar alloy  $\text{Fe}_{64.6}\text{Ni}_{35.4}$ . We have performed Fe and Ni *K*-edge extended x-ray-absorption fine-structure (EXAFS) spectroscopic measurements and the computational simulations based on the path-integral effective-classical-potential (PIECP) theory.

Figure 2(a) show the cohesive energies of hypothetical *fcc* Fe and the Invar alloy as a function of the lattice distance. In the present atomic potentials, *fcc* Fe shows that the LS state is more stable by 8.0 meV than the HS state, while the Invar case exhibits a more stable HS state by 25.0 meV. The bond distances of the HS and LS states are around  $R_{\text{HS}} = 2.530 \text{ \AA}$  and  $R_{\text{LS}} = 2.490 \text{ \AA}$ , respectively. Figures 2(b) and 2(c) show the

first nearest-neighbor (NN) shells around Fe and Ni, respectively. Those around Fe show almost no thermal expansion, while those around Ni exhibit meaningful but smaller expansion than that of *fcc* Ni. At low temperature (< 100 K), the quantum effect is found to play an essentially important role. This is confirmed by comparing the quantum-mechanical simulations to the classical ones, the latter of which exhibit large (normal) thermal expansion at low temperature.

It is also revealed that thermal expansion for the Ni–Ni and Ni–Fe pairs is noticeably suppressed, even though the Ni electronic state may not vary depending on the temperature. On the other hand, the anharmonicity (asymmetric distribution) clearly exists for all the first NN shells as in the case of the normal thermal expansion system, where thermal expansion originates almost exclusively from the anharmonic interatomic potential. This implies the breakdown of the direct correspondence between thermal expansion and anharmonicity in a simple two-body model.

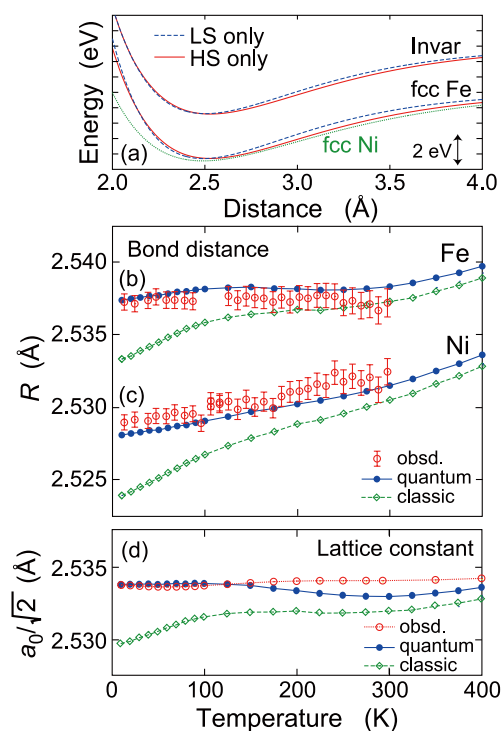


**Figure 2.** (a) Cohesive energies of Invar  $\text{Fe}_{64.6}\text{Ni}_{35.4}$  (top lines), *fcc* Fe (bottom lines), and *fcc* Ni (bottom, green dotted line) as a function of the 1st NN distance at a temperature of 0 K. For Fe, two types of the potentials for the HS (red solid line) and LS (blue dashed line) states are depicted. (b),(c) Simulated 1st NN bond distance around Fe (b) and Ni (c) given by the PIECP (blue circles and solid line, quantum) and the classical MC (green diamond and dashed line, classic) methods, together with the experimental EXAFS data (red open circle with an error bar). (d) Equilibrium 1st NN distance ( $a_0/\sqrt{2}$ ) given by the PIECP and classical MC simulations, together with the experimental literature data (red circle and dotted line).

### Reference

- 1) T. Yokoyama and K. Eguchi, *Phys. Rev. Lett.* **107**, 065901 (2011).

# Design and In-Situ Characterization of Catalyst Surfaces

Department of Materials Molecular Science  
Division of Electronic Structure



TADA, Mizuki  
MURATSUGU, Satoshi  
WENG, Zhihuan  
MAITY, Niladri  
ZHANG, Shenghong  
WATTANAKIT, Chularat  
TABTHONG, Sittichoke  
THUMRONGPATANARAKS, Wipavee  
GAN, Raymond  
JIANG, Lu  
WANG, Fei  
SAIDA, Takahiro  
ISHIGURO, Nozomu  
KUSHIDA, Yuko  
VU, Thang  
FUNAKI, Yukino  
USUI, Chika  
GONDO, Makiko  
FUKUTOMI, Yukiyo

Associate Professor  
Assistant Professor  
Post-Doctoral Fellow  
Post-Doctoral Fellow  
Post-Doctoral Fellow  
Visiting Scientist  
Visiting Scientist  
Visiting Scientist  
Visiting Scientist  
Visiting Scientist  
Graduate Student  
Graduate Student\*  
Graduate Student†  
Graduate Student†  
Graduate Student†  
Technical Fellow  
Technical Fellow  
Technical Fellow  
Secretary

## 1. Preparation of Molecularly Imprinted Ru-Complex Catalysts for Asymmetric Transfer Hydrogenation in Water

We have prepared molecularly imprinted metal-complex catalysts on oxide surfaces, whose ligand is utilized as a template. A molecularly imprinted cavity memorized the shape and coordination environment of a template ligand can be prepared on a catalytically active metal complex behind the template from the supported metal complex. We have prepared molecularly imprinted Ru-complex catalysts on a SiO<sub>2</sub> surface for asymmetric transfer hydrogenation in water by stacking of organic polymer-matrix overlayers on the SiO<sub>2</sub> surface for the molecular imprinting of the supported Ru complex.

Molecularly imprinted Ru-complex catalysts were prepared by step-by-step procedures illustrated in Figure 1: (1) the attachment of a Ru complex on SiO<sub>2</sub>, (2) the coordination of a template ligand ((*R*)-1-(*o*-fluorophenyl)ethanol), which is the product of *o*-fluoroacetophenone hydrogenation, (3) stacking of surface matrix overlayers using organic or inorganic polymer matrices, and (4) the removal of the template ligand from the Ru complex. We utilized hydrophobic organic polymer matrices for the transfer hydrogenation in water media and conducted several methods to prepare surface matrix overlayers on SiO<sub>2</sub>: (a) photopolymerization of ThreeBond 3026E containing acrylate oligomer and 2-hydroxyethyl methacrylate, (b) vapor deposition polymerization of styrene and divinylbenzene, (c) precipitation polymerization of methylmethacrylate and ethyleneglycol dimethacrylate, and

(d) hydrolysis-polymerization of tetramethoxysilane. The structures of the supported and molecularly imprinted Ru catalysts were characterized by XPS, solid-state NMR, XRF, TGA, UV/vis, and Ru K-edge XAFS.

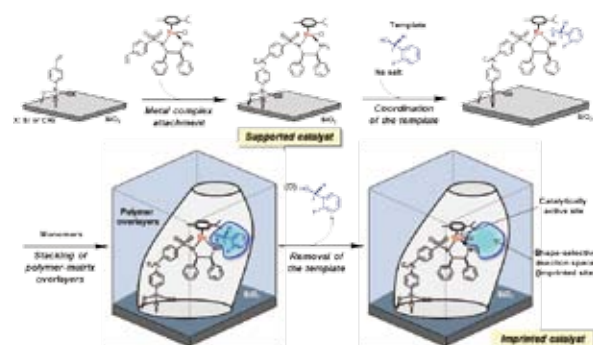


**Figure 1.** Preparation scheme of a molecularly imprinted Ru-complex catalyst on SiO<sub>2</sub> for the transfer hydrogenation of *o*-fluoroacetophenone in water.

XPS peak intensity analysis of Si 2p to C 1s of the polymer-stacked Ru catalysts showed that the stacking manner of these polymer matrices on the SiO<sub>2</sub> surface were significantly different. In the case of the photopolymerization of ThreeBond 3026E, we found large decrease in the peak intensity ratio, indicating that space around the supported Ru complex was covered by the polymer matrices. The stacking of the matrix overlayers changed catalytic behaviors for the *o*-fluoroaceto-

phenone transfer hydrogenation in water and the improvement of enantioselectivity was observed.

## 2. Space-Resolved XAFS Analysis of A Single Catalyst Particle of A Supported Ni Catalyst Using X-Ray $\mu$ -Beam

Catalytic performances of solid catalysts depend on the structural and electronic aspects (oxidation state, coordination symmetry, local coordination structure, *etc.*) of catalysts, which are generally inhomogeneous powder assembly of solid particles with nm– $\mu$ m sizes. X-ray beam for conventional XAFS (X-ray Absorption Fine Structure) is typically in mm size, which obtains macroscopically averaged structural information on the assembly of heterogeneous catalyst particles with various sizes, composition, and structures within mm-sized X-ray beam-spot. Structural bond information around a particular catalytic element in an individual catalyst particle has not been reported well because of the lack of characterization techniques with fine space resolution to directly observe such structural parameters of a single catalyst particle.

We have investigated the structural information of a single catalyst particle of a supported Ni catalyst ( $\text{NiO}_x/\text{Ce}_2\text{Zr}_2\text{O}_y$ ,  $0 \leq x \leq 1$ ,  $7 \leq y \leq 8$ ) for  $\text{CH}_4$  steam reforming by 2-dimensional scanning  $\mu$ -XRF and  $\mu$ -XAFS analysis using an X-ray  $\mu$ -beam ( $1000 \text{ nm } (h) \times 800 \text{ nm } (v)$ ). X-ray beam at Ni K-edge (8332 eV) was focused by Kirkpartick-Baez (KB) mirrors at the BL37XU beamline at SPring-8. The catalyst particles (average particle size =  $750 \pm 370 \text{ nm}$ ) were dispersed on a thin  $\text{SiO}_2$  membrane substrate and the membrane was mounted on a piezoelectric translation stage for scanning  $\mu$ -XRF and  $\mu$ -XAFS. Fluorescent X-rays emitted from the sample were detected by a 19-element Ge detector.

2-Dimensional scanning  $\mu$ -XRF mapping showed the position of each catalyst particle on the  $\text{SiO}_2$  substrate (Figure 2 (A)). Significant contrast of the Ni  $K\alpha$  and Ce  $L\alpha + L\beta$  fluorescent X-rays was observed as shown in Figure 2 (A) and the size of the high X-ray intensity area was consistent to the size of the catalyst particles. Ni K-edge  $\mu$ -XANES of both  $\text{Ni}/\text{Ce}_2\text{Zr}_2\text{O}_7$ , which was active for the  $\text{CH}_4$  steam reforming, and  $\text{NiO}/\text{Ce}_2\text{Zr}_2\text{O}_8$ , which was inactive for the reaction, were measured at the positions of the catalyst particles, and the  $\mu$ -XANES spectra of the both catalysts were significantly different each other as shown in Figure 2 (B) ((a) and (c)).

Figure 2 (C) shows a Ni K-edge  $\mu$ -EXAFS Fourier transform of a single catalyst particle of the inactive  $\text{NiO}/\text{Ce}_2\text{Zr}_2\text{O}_8$ , recorded for 3 h. To our knowledge, the local

coordination structure of the supported Ni species on a single catalyst particle was successfully analyzed for the first time by  $\mu$ -EXAFS with the spatial resolution to the size of the catalyst particle. The Ni K-edge  $\mu$ -EXAFS analysis of  $\text{NiO}/\text{Ce}_2\text{Zr}_2\text{O}_8$  revealed the local coordination of the catalytically inactive Ni species (Ni–O and Ni–Ni), which was attributed to the NiO species. The  $\mu$ -XAFS technique would be promising to explore new *in situ* space-resolved catalysis science, to understand catalysis of a single nanoparticle excluding noise information from the heterogeneous properties of the catalyst particle assembly.

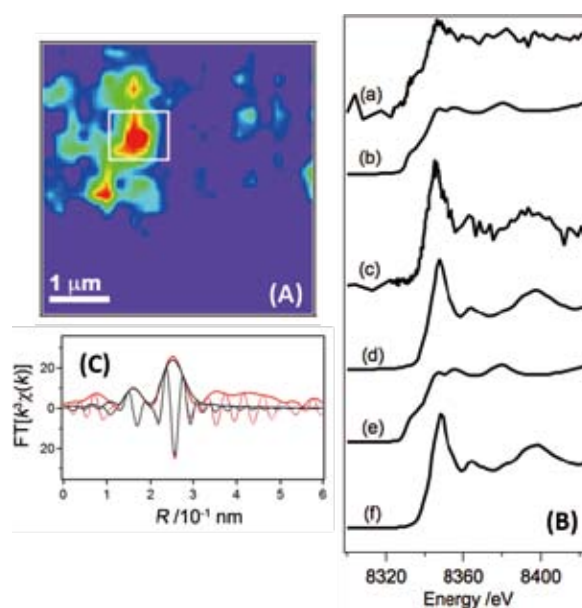


**Figure 2.** (A) A 2D-scanning Ni  $K\alpha$  XRF mapping image of  $\text{Ni}/\text{Ce}_2\text{Zr}_2\text{O}_7$ . 1 pixel = 200 nm. A white square in the image represents the beam area of (B)-(a). (B) Ni K-edge XANES spectra: (a)  $\mu$ -XANES of a  $\text{Ni}/\text{Ce}_2\text{Zr}_2\text{O}_7$  particle, (b) conventional XANES of  $\text{Ni}/\text{Ce}_2\text{Zr}_2\text{O}_7$  powder assembly, (c)  $\mu$ -XANES of a  $\text{NiO}/\text{Ce}_2\text{Zr}_2\text{O}_8$  particle, (d) conventional XANES of  $\text{NiO}/\text{Ce}_2\text{Zr}_2\text{O}_8$  powder assembly, (e) Ni foil, and (f) NiO. (C) Ni K-edge Fourier transform of a  $\text{NiO}/\text{Ce}_2\text{Zr}_2\text{O}_8$  catalyst particle. Red and black lines represent on the observed and fitted spectra.

### References

- 1) Z. Weng, S. Muratsugu, N. Ishiguro, S. Ohkoshi and M. Tada, *Dalton Trans.* **40**, 2338–2347 (2011).
- 2) M. Tada, N. Ishiguro, T. Uruga, H. Tanida, Y. Terada, S. Nagamatsu, Y. Iwasawa and S. Ohkoshi, *Phys. Chem. Chem. Phys.* **13**, 14910–14913 (2011).

\* carrying out graduate research on Cooperative Education Program of IMS with Sinshu University

† carrying out graduate research on Cooperative Education Program of IMS with The University of Tokyo

‡ carrying out graduate research on Cooperative Education Program of IMS with JAIST

# Studies of Charge-Order State in Organic Conductors

Department of Materials Molecular Science  
Division of Electronic Properties



YAKUSHI, Kyuya  
YAMAMOTO, Kaoru  
URUICHI, Miki  
YUE, Yue  
ABE, Hitomi

Professor\*  
Assistant Professor  
Technical Associate  
Post-Doctoral Fellow  
Secretary

In organic conductors, kinetic energy is comparable with on-site and inter-site Coulomb energy. Due to this reason, many organic conductors are located in a boundary area between metallic and insulating states, and thus various organic charge-transfer compounds show metal–insulator phase transition. Recently, charge-ordered (CO) state originated from interelectron Coulomb interaction is widely found in organic conductors. The CO state attracts attention, first because charge-fluctuation-mediated superconductivity is theoretically predicted in superconducting compounds neighbored on CO phase, second because some compounds in CO phase show ferroelectricity. The macroscopic polarization in this ferroelectric transition is recognized not as the result of ionic displacements, but as the result of coherent integration of electronic polarizations induced by the CO transition. We have investigated the CO state and metallic state near CO employing infrared and Raman spectroscopy and SHG microscopy.

## 1. Hydrogen Isotope Effect on the Charge-Ordering Phase Transition in $\alpha'$ -(BEDT-TTF)<sub>2</sub>IBr<sub>2</sub>

$\alpha'$ -(BEDT-TTF)<sub>2</sub>IBr<sub>2</sub> has a layered structure with two-dimensional interaction within the layer. In a variety of organic conductors,  $\alpha'$ -(BEDT-TTF)<sub>2</sub>IBr<sub>2</sub> is one of the most narrow-bandwidth compounds. Because of the narrow-bandwidth, the charge carriers of this compound is localized, and thus  $\alpha'$ -(BEDT-TTF)<sub>2</sub>IBr<sub>2</sub> is an insulator in a whole temperature range from 350 K to 4.2 K. This insulating compound shows successive phase transitions at 207 K, ~160 K, and ~30 K. The resistivity jump at 207 K is regarded as an order-disorder phase transition of localized holes.<sup>1)</sup> Below ~160 K, macroscopic polarization evolves, suggesting a ferroelectric phase transition. Finally this compound undergoes a first order magnetic phase transition at ~30 K. Our goal is to understand the mechanism of this successive phase transition. In this section, we focus on the hydrogen isotope effect on the order-disorder phase transition at 207 K.

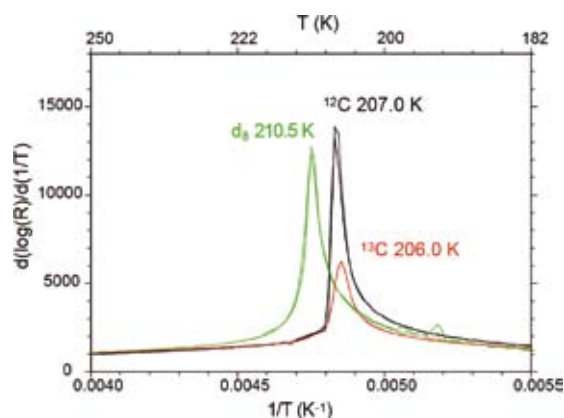


**Figure 1.** Comparison of the derivatives of electrical resistivity of  $\alpha'$ -(BEDT-TTF)<sub>2</sub>IBr<sub>2</sub>, deuterium-substituted compound,  $\alpha'$ -(d<sub>8</sub>-BEDT-TTF)<sub>2</sub>IBr<sub>2</sub>, and <sup>13</sup>C-substituted compound,  $\alpha'$ -(<sup>13</sup>C-BEDT-TTF)<sub>2</sub>IBr<sub>2</sub> where <sup>13</sup>C is substituted at the central C=C bond of BEDT-TTF.  $\alpha'$ -(d<sub>8</sub>-BEDT-TTF)<sub>2</sub>IBr<sub>2</sub> shows a significant isotope effect on the order-disorder phase transition.

Figure 1 shows the derivative of the electrical resistance,  $d(\log R)/d(1/T)$ , where the peak temperature corresponds to the phase transition temperature,  $T_C$ . As shown in this figure,  $T_C$  of  $\alpha'$ -(d<sub>8</sub>-BEDT-TTF)<sub>2</sub>IBr<sub>2</sub> shows a high-temperature shift of 3–4 K. The unit cell volume of  $\alpha'$ -(d<sub>8</sub>-BEDT-TTF)<sub>2</sub>IBr<sub>2</sub> shrinks by about 0.4% compared with that of  $\alpha'$ -(BEDT-TTF)<sub>2</sub>IBr<sub>2</sub>. The volume change can be regarded as the result of chemical pressure. If we assume that the chemical pressure pushes up  $T_C$ , the isotope shift means  $dT_C/dP > 0$ . However, this assumption is opposite to the experimentally obtained pressure dependence of  $T_C$ ,  $dT_C/dP < 0$ .<sup>1)</sup> Therefore, the isotope effect cannot be attributed to the effect of chemical pressure. We therefore propose a small polaron model, in which the effective transfer integral is reduced as  $\tilde{t} = t \exp(-S)$ , where  $S = (E_b/\hbar\omega_0) \coth(\hbar\omega_0/2kT)$  is a vibrational overlap factor (Huang-Rhys factor). The deuterium substitution may soften the optical phonon mode  $\omega_0$ , and increases  $S$ . This effect reduces the effective transfer integral, and thus the

bandwidth. The decrease of bandwidth is regarded as the application of negative pressure. Combined with the relationship,  $dT_c/dP < 0$ , this small polaron model can qualitatively explain the isotope effect on the phase transition. We speculate that the librational modes around the short axis and the axis perpendicular to the molecular plane work most effectively as the optical phonon  $\omega_0$ .

## 2. Inhomogeneous Ferroelectric Polarization in $\alpha'$ -(BEDT-TTF)<sub>2</sub>IBr<sub>2</sub> Revealed by Second-Harmonic Generation Microscopy<sup>2)</sup>

As an effort to expand the material family of unconventional class of ferroelectrics, we focused in the present study on  $\alpha'$ -(BEDT-TTF)<sub>2</sub>IBr<sub>2</sub>, which is another BEDT-TTF complex with trihalide anions similar to  $\alpha$ -(BEDT-TTF)<sub>2</sub>I<sub>3</sub>. As expected from the similarity in the crystal structure, we have confirmed that the complex shows charge ordering at low temperatures<sup>1)</sup> in a separate study. The result of SHG measurements indeed verified that the complex also showed SHG in a charge-ordered phase, though the transition features of the complex turned out to be substantially different from those of the triiodide complex.

One of the interesting features is an inhomogeneous generation of SH signal from a single crystal, revealed by mapping measurement of SHG. The spatially resolved observation was performed for a filmy singly crystal ( $t = ca. 3 \mu\text{m}$ ) in transmission geometry using a homemade scanning laser microscope equipped with an Er-doped fiber laser ( $\lambda = 1.55 \mu\text{m}$ , pulse duration: 100 fs, repetition: 20 MHz). The laser beam was focused by an objective lens into a spot ( $\phi = ca. 20 \mu\text{m}$ ) on the  $ab$ -plane of the crystal with an excitation power density of less than  $ca. 500 \text{ W/cm}^2$ . To efficiently dissipate the heat at the spot, the crystal was embedded in polymer resin, afterwards sandwiched by a pair of two sapphire slides, then cooled by a liquid He flowing cryostat.

Figure 2 shows the comparison of the transmission and SHG images of the single crystal. As shown by the crack observed in the transmission image [Figure 2(a)], the crystal was cleaved together with the polymer matrix when cooled. As is displayed in Figure 2(b), the SHG image shows uneven distribution of the nonlinear optical signal; the signal was emanated from limited regions near the cracks and the edges of the crystal, whereas other regions far from cracks are almost completely dark.

Note that the SHG signal is generated not only from the very end of the crystal edges at the crack, but regions with a

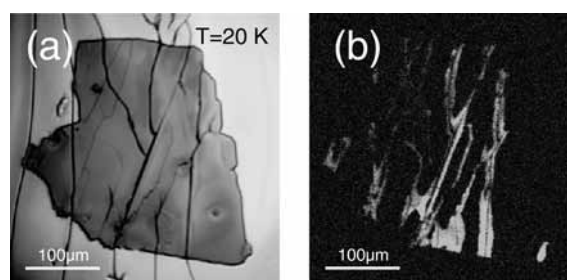


**Figure 2.** (a) Transmission image of a single crystal of  $\alpha'$ -(BEDT-TTF)<sub>2</sub>IBr<sub>2</sub> embedded in polymer resin, and (b) its SH image measured at 20 K. The SHG intensity in (b) is in proportional to the brightness.

macroscopic width. This clearly indicates that the activation of SHG is not caused by the surface effect at the crack, but should be a manifestation of the breakdown of centrosymmetry in the bulk region. The uneven signal distribution is presumably attributed to inhomogeneous pressure distribution associated with the crack in polymer matrix generating at low temperatures; the matrix adhering to a sapphire plate should feel a stretching force (since the thermal expansion coefficient of the polymer is larger than sapphire), whereas the region near the crack would be free from the stretching force. Hence, the region near the crack, emanating the SHG light, seems to represent the ambient pressure property of the bulk state.

The coexistence of the dark region in the image would be noteworthy. This indicates that the generation of the ferroelectric polarization is suppressed presumably by a small negative pressure, suggesting that a non-polar phase exists near the ferroelectric CO phase in the phase diagram. One may notice that the bright and dark regions are divided by clear boundaries, which fact implies that these two phases would be separated by a first-order transition.

The appearance of the distinct phases strongly suggests that there would be several stable arrangements for the charge order as realized for the spin system with geometrical frustration. To understand the intriguing features of the ferroelectric transition in this compound, precise crystal geometry at low temperatures as well as the SHG data measured without application of mechanical stress is necessary.

### References

- 1) Y. Yue, *et al.*, *J. Phys. Soc.* **78**, 044701 (2009).
- 2) K. Yamamoto *et al.*, *Physica B* **405**, S363 (2010).
- 3) K. Yamamoto, *et al.*, *J. Phys. Soc. Jpn.* **77**, 074709 (2008).

### Award

YAMAMOTO, Kaoru; JPSJ Award Article 2011.

\* Present Address; Toyota Physical and Chemical Research Institute

# Magnetic Resonance Studies for Molecular-Based Conductors

Department of Materials Molecular Science  
Division of Electronic Properties



NAKAMURA, Toshikazu Associate Professor  
FURUKAWA, Ko Assistant Professor  
SUGIURA, Koichi Graduate Student  
ABE, Hitomi Secretary

Magnetic resonance measurements are advantageous for studying fundamental electronic properties and for understanding the detailed electronic structures of molecular based compounds. Developing an understanding of the electronic phases and functionality of these materials enables us to perform systematic investigations of low-dimensional, highly-correlated electron systems and functional materials. Competition between the electronic phases in molecular-based conductors has attracted much attention. The investigations of such electronic phases by magnetic resonance measurements are important to understanding unsolved fundamental problems in the field of solid state physics, and to explore novel functionalities in the field of material science.

In this study, we performed broad-line NMR and ESR measurements on molecular-based conductors to understand electron spin dynamics and functionality in low-temperature electronic phases.

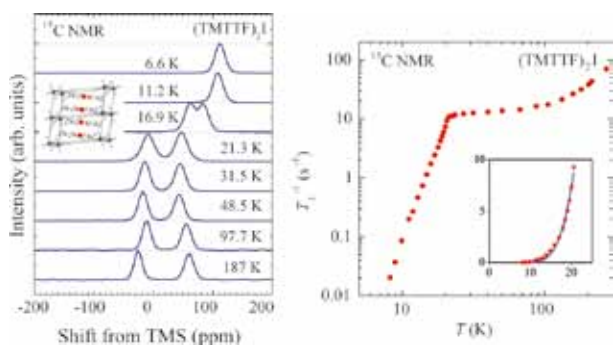


**Figure 1.** (Left) Temperature dependence of the  $^{13}\text{C}$ -NMR spectra of a single crystal of  $(\text{TMTTF})_2\text{I}$ . Frequencies are referenced against tetramethylsilane. (Right) Temperature dependence of the  $^{13}\text{C}$ -NMR, spin-lattice relaxation rate,  $T_1^{-1}$ , of  $(\text{TMTTF})_2\text{I}$ . The inset is the low-temperature region, drawn with a linear scale. The blue line shows fitting results that assumed a simple gap, with  $\Delta \sim 128$  K.

## 1. Structural Investigation of the Spin-Singlet Phase in $(\text{TMTTF})_2\text{I}$

To elucidate the electronic state that exists in the boundary region between the spin-singlet phase and the high-pressure side antiferromagnetic phase in the modified generalized phase diagram, we carried out x-ray diffraction, electron spin resonance, and nuclear magnetic resonance measurements of the tetramethyl-tetrathiafulvalene (TMTTF) family salt,  $(\text{TMTTF})_2\text{I}$ . The unit-cell volume of  $(\text{TMTTF})_2\text{I}$  is between that of  $(\text{TMTTF})_2\text{Br}$  and  $(\text{TMTTF})_2\text{PF}_6$ . We found that  $(\text{TMTTF})_2\text{I}$  undergoes a spin-singlet phase transition at 21 K without involving paramagnetic charge-ordering phase. Therefore, the charge-ordering transition is not necessary for the spin-singlet transition of TMTTF salts as seen in other conventional spin-singlet salts. Finally, we discuss possible mechanisms of the spin-singlet phase transition.

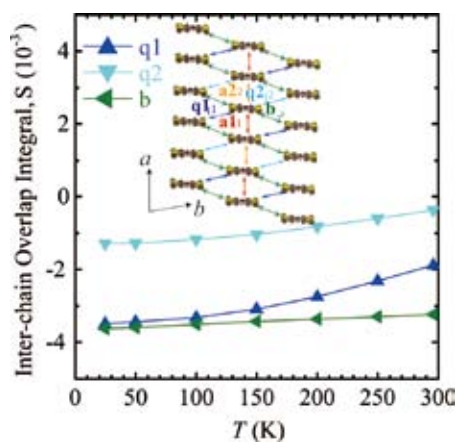


**Figure 2.** Temperature dependence of the overlap integral of  $(\text{TMTTF})_2\text{I}$  down to 25 K focusing on the inter-chain overlap integral. The overlap parameters within the  $ab$ -plane are defined in the inset.

## 2. Photoinduced Triplet States of Photoconductive TTF Derivatives Including a Fluorescent Group

The spin dynamics of photoconductive tetrathiafulvalene (TTF) derivatives containing 2,5-diphenyl-1,3,4-oxadiazole (PPD) was examined using time-resolved electron spin resonance (TR-ESR) spectroscopy. TR-ESR signals of a frozen solution sample under visible excitation were attributed to the excited triplet state  $T_1$ , which was populated via intersystem crossing from the excited singlet state  $S_1$  as confirmed by TR-ESR spectral simulations. From DFT calculations, the spin density distribution of the  $T_1$  state was found to be concentrated around the linker between the TTF and PPD molecules.

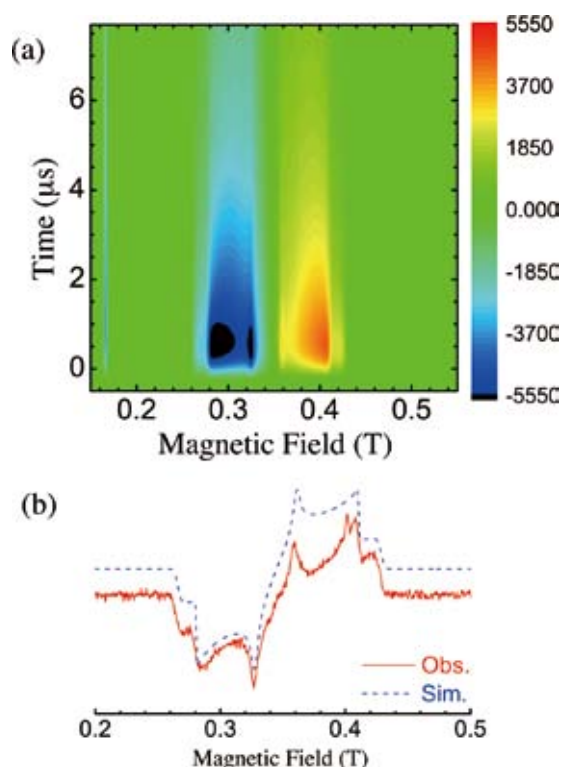


**Figure 3.** (a) 2D pulsed TR-ESR spectra for photoconductive TTF derivatives containing PPD. The normal axis represents the ESR signal intensity. The color scale denotes the signal intensity. Positive and negative values indicate the absorption and emission of microwaves, respectively. (b) Slice spectra along the magnetic field axis at  $t = 0.5 \mu\text{s}$  and  $T = 20 \text{ K}$ . The solid and dotted lines denote the observed and simulated spectra, respectively.

## 3. Magnetic Memory Based on Magnetic Alignment of a Paramagnetic Ionic Liquid near Room Temperature

A paramagnetic ferrocenium-based ionic liquid that exhibits a magnetic memory effect coupled with a liquid–solid phase transformation has been developed. Based on field

alignment of the magnetically anisotropic ferrocenium cation, the magnetic susceptibility in the solid state can be tuned by the weak magnetic fields ( $< 1 \text{ T}$ ) of permanent magnets.

## 4. Completely Hydrostatic Pressure Effect of Anisotropic Resistivity in the 1-D Organic Conductor $(\text{TMTTF})_2\text{SbF}_6$

The anisotropic resistivity of  $(\text{TMTTF})_2\text{SbF}_6$  under hydrostatic pressure was investigated up to  $\sim 0.3 \text{ GPa}$  using a helium gas pressure control system. The resistivity along the  $a$  axis shows a metallic behavior above a crossover temperature  $T_p$  ( $\sim 220 \text{ K}$  at ambient pressure) and an insulating behavior below  $T_p$ . On the other hand, the temperature dependence of  $\rho_b$  and  $\rho_c$  was found to show a kink at a charge ordered temperature  $T_{CO}$ . Interestingly,  $T_p$  was increased with applying pressure while  $T_{CO}$  was decreased with applying pressure. We discuss this unusual feature in terms of the pressure–temperature phase diagram in the  $(\text{TMTCF})_2\text{X}$  system.

## 5. $^{13}\text{C}$ NMR Study of the Magnetic Properties of the Quasi-One-Dimensional Conductor, $(\text{TMTTF})_2\text{SbF}_6$

Magnetic properties in the quasi-one-dimensional organic salt  $(\text{TMTTF})_2\text{SbF}_6$  are investigated by  $^{13}\text{C}$  NMR under pressures. Antiferromagnetic phase transition at ambient pressure (AFI) is confirmed. Charge-ordering is suppressed by pressure and is not observed under 8 kbar. For  $5 < P < 20 \text{ kbar}$ , a sharp spectrum and the rapid decrease of the spin-lattice relaxation rate  $1/T_1$  were observed below about 4 K, attributed to a spin-gap transition. However, as the reduction of the Knight shift was not observed, the phase is not conventional non-magnetic spin-Peierls. Above 20 kbar, extremely broadened spectrum and critical increase of  $1/T_1$  were observed. This indicates that the system enters into another antiferromagnetic phase (AFII) under pressure. The slope of the antiferromagnetic phase transition temperature  $T_{AFII}$ ,  $dT_{AFII}/dP$ , is positive, while  $T_{AFI}$  decreases with pressure. The magnetic moment is weakly incommensurate with the lattice at 30 kbar.

### References

- 1) K. Furukawa, K. Sugiura, F. Iwase and T. Nakamura, *Phys. Rev. B* **83**, 184419 (5 pages) (2011).
- 2) K. Furukawa, Y. Sugishima, H. Fujiwara and T. Nakamura, *Chem. Lett.* **40**, 292–294 (2011).
- 3) Y. Funasako, T. Mochida, T. Inagaki, T. Sakurai, H. Ohta, K. Furukawa and T. Nakamura, *Chem. Commun.* **47**, 4475–4477 (2011).
- 4) M. Itoi, Y. Ishii, H. Kitano, S. Takekoshi, K. Matsubayashi, Y. Uwatoko and T. Nakamura, *Physica C* **470**, S594–S595 (2011).

# Design of Porous Polymer Frameworks

Department of Materials Molecular Science  
Division of Molecular Functions



JIANG, Donglin  
NAGAI, Atsushi  
KOU, Yan  
LIU, Xiaoming  
GUO, Zhaoqi  
XU, Yanhong  
DING, Xuesong  
JIN, Shangbin  
CHEN, Xiong  
FENG, Xiao  
CHEN, Long  
SUZUKI, Hiroko

Associate Professor  
Assistant Professor  
Post-Doctoral Fellow  
Post-Doctoral Fellow  
Post-Doctoral Fellow  
Graduate Student  
Graduate Student  
Graduate Student  
Graduate Student  
Graduate Student  
Secretary

Covalent organic frameworks (COFs) are a new class of porous architectures that allow the integration of organic units with atomic precision into long-range-ordered two and three-dimensional structures. From a synthetic point of view, COFs are intriguing since they allow a new degree of control of porosity, composition and component positions. However, the construction of COFs to date has been limited to certain monomers, and the lack of suitable protocols utilizing other units has impeded further advances in this emerging field. To advance this emerging field it is important to extend the limited number of synthetic protocols and monomer units available. In our group, we have developed various  $\pi$ -electronic 2D COFs with porphyrin and phthalocyanine.<sup>1-3)</sup>

Conjugated microporous polymers (CMPs) are another class of porous frameworks consisting of extended  $\pi$ -conjugation and inherent nanopores. As high surface-area porous materials, CMPs emerge as a new medium for gas adsorption and have been developed as a new type of nanoreactors and heterogeneous catalysts upon the integration of catalytic sites into the skeletons.<sup>4)</sup> From a synthetic point of view, CMPs are unique because they allow the elaborate control of both skeletons and pores. In this context, a promising way to the exploration of CMPs is to combine the structural advantages of being  $\pi$ -conjugation and possessing inherent pores. We have developed such a cooperative porous framework based on aza-fused CMPs for supercapacitive energy storage and electric power supply.<sup>5)</sup>

## 1. Two-Dimensional Phthalocyanine Polymer and Covalent Organic Framework

NiPc-COF was synthesized by the boronate esterification reaction of  $(\text{OH})_8\text{NiPc}$  and 1,4-benzene diboronic acid (BDDBA) in dimethylacetamide (DMAc)/*o*-dichlorobenzene under solvothermal conditions (Figure 1a). PXRD patterns of NiPc-COF exhibited strong diffraction peaks at  $3.78^\circ$ ,  $7.72^\circ$ ,  $11.56^\circ$  and  $26.62^\circ$  assignable to 100, 200, 300 and 001 facets, respectively. Based on the PXRD pattern, the center-to-center

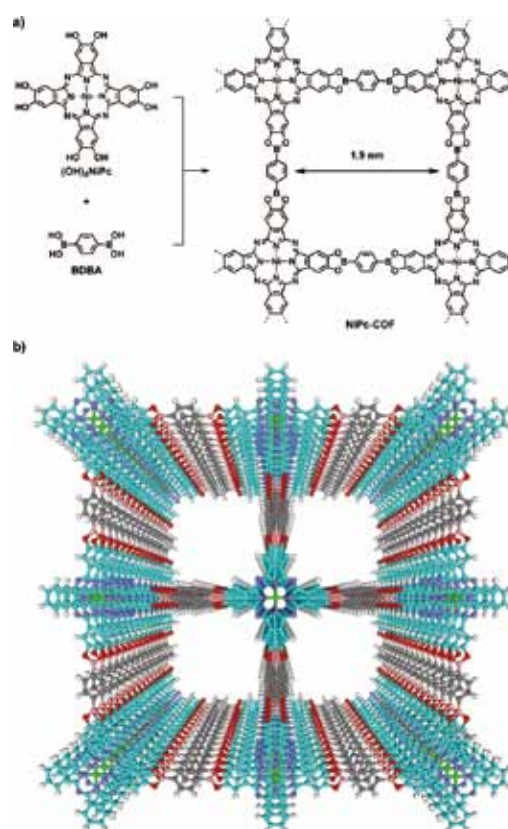


**Figure 1.** a) Schematic representation of the synthesis of NiPc-COF based on boronate esterification reaction. b) Eclipsed stack of phthalocyanine 2D sheets and microporous channels in NiPc-COF ( $a \times 2$  grid). Colors used for identification are as follows: phthalocyanine unit (sky blue), Ni (green), N (violet), C (grey), O (red), B (orange) and H (white).

distance between neighboring pores was evaluated as 2.36 nm and the separation between the sheets as  $3.32 \text{ \AA}$ . Simulations using the  $P4/mmm$  space group with  $a = b = 23.12247 \text{ \AA}$  and  $c = 3.36358 \text{ \AA}$  gave a PXRD pattern in good agreement with the experimentally observed pattern. The phthalocyanine units are

located at nodes separated by 2.3 nm in the 2D plane and stack to form layers separated by a distance of 3.36 Å. In contrast, the staggered arrangement resulting from an *I4* space group did not reproduce the experimental pattern. In this stacking, the phthalocyanine units overlap on the pores of the neighboring planes.

Owing to ordered stacking of the phthalocyanine units, NiPc-COF becomes photoconductive, generating a prominent photocurrent. Irradiation from a Xenon light source (> 400 nm) with a UV cut-off module resulted in a significant increase in current from 20 nA (dark current) to 3 μA (photocurrent). Further, on-off switching experiments showed that NiPc-COF quickly responded to light irradiation and that the photocurrent can be switched on and off many times without deterioration. In contrast, (MeO)<sub>8</sub>NiPc did not show any photoresponse under the same conditions. To investigate the wavelength dependence of the photosensitivity, we irradiated with light passed through band-pass filters ( $\pm 5$  nm). NiPc-COF was panchromatically responsive to different wavelengths and was extremely sensitive to deep-red and near-infrared photons. The increased light-harvesting capability and enhanced carrier mobility accounts for the high photoconductivity and sensitivity. Therefore, owing to well-ordered stacking of the phthalocyanine unit, NiPc-COF shows enhanced light-harvesting capability in the visible and near-infrared regions, is semi-conducting and facilitates charge carrier transport. NiPc-COF is highly photoconductive, exhibiting a panchromatic light response and exceptional sensitivity to visible and near-infrared photons. These properties are unique and highly correlated with the structure of NiPc-COF. The remarkable results demonstrate the enormous potential of two-dimensional polymers in novel optoelectronics applications.

## 2. Aza-Fused Conjugated Microporous Polymers for Supercapacitive Energy Storage and Electric Power Supply

Supercapacitors are energy storage and power supply devices that are in increasing demand with the broadening of applications such as vehicles and electric devices. Supercapacitive energy storage operates on the electric double layer by accumulation of charges at the electrode/electrolyte interface, where the stored energy is proportional to the capacitance of the electrode. Therefore, a breakthrough in the electrode materials holds the key to fundamental advances in supercapacitors. Despite the extensive efforts in synthesis, the rational design of supercapacitive electrodes that meet large capacitance, high energy density, and outstanding stability remains a substantial challenge.

Aza-CMPs were synthesized by the condensation reaction of 1,2,4,5-benzenetetramine with triquinoyl hydrate (Figure 2, Aza-CMPs). Aza-CMPs comprise four features: (1) fused CMP frameworks that are conductive, (2) aza units in the skeletons that enable dipolar interaction with electrolyte

cations and accumulate protons on the walls of pores, (3) inherent micropores with optimized size that allows quick ion motion during charge-discharge processes, and (4) high surface area provide large interface for the formation of electrostatic charge-separation layers in the pores. Ultimately, these structural features work cooperatively, leading to exceptional energy storage and power supply capacities.

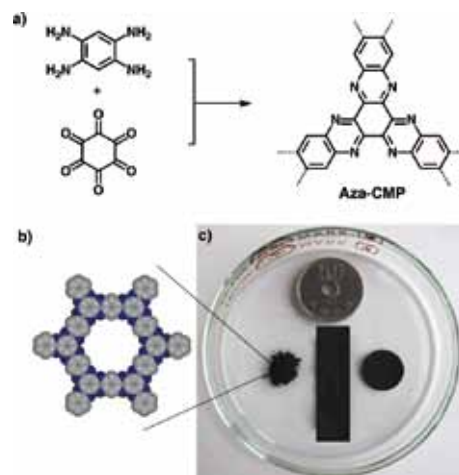


**Figure 2.** a) Schematic representation of the synthesis of Aza-CMP. b) The elementary pore structure of Aza-CMPs (grey is carbon network and blue is nitrogen). c) Photographic image of the powder and flexible thin films with different shapes of Aza-CMPs.

We have explored CMPs for supercapacitive energy storage, through the construction of an aza-fused porous framework with built-in aza units and high surface-area micropores. The fused skeleton, dense aza units, and well-defined micropores work cooperatively and facilitate electrostatic charge-separation layer formation. Consequently, Aza-CMPs exhibit large capacitance, high energy and power densities, and enable repetitive energy storage and power supply with excellent cycling life. These remarkable results demonstrate the enormous potential of conjugated microporous polymers in the exploration of energy materials.

### References

- 1) X. Ding, L. Chen, Y. Honsho, X. Feng, O. Saengsawang, J. Guo, A. Saeki, S. Seki, S. Irie, S. Nagase, P. Vudhichai and D. Jiang, *J. Am. Chem. Soc.* **133**, in press (2011).
- 2) X. Feng, L. Chen, Y. Dong and D. Jiang, *Chem. Commun.* **47**, 1979–1981 (2011).
- 3) X. Ding, J. Guo, X. Feng, Y. Honsho, J. Guo, S. Seki, P. Maitarad, A. Saeki, S. Nagase and D. Jiang, *Angew. Chem., Int. Ed.* **50**, 1289–1293 (2011).
- 4) Y. Kou, Y. Xu, Z. Guo and D. Jiang, *Angew. Chem., Int. Ed.* **50**, 8753–8757 (2011). (VIP)
- 5) L. Chen, Y. Yang, Z. Guo and D. Jiang, *Adv. Mater.* **23**, 3149–3154 (2011).

# Solid State NMR for Structural Biology

Department of Materials Molecular Science  
Division of Molecular Functions



NISHIMURA, Katsuyuki Associate Professor  
IIJIMA, Takahiro Assistant Professor  
TANIO, Michikazu IMS Research Assistant Professor

We are working on methodology and hardware developments of solid state NMR and structural biology based on them. In the following, we show developed variable temperature (VT) magic angle spinning (MAS) probe for ultra high field NMR and preliminary result of newly constructed over expression system of a peripheral membrane protein. In addition, a dynamics study of paramagnetic compound was reported.

## 1. Development of VT-MAS Solid-State NMR Probe for Ultra High Field 920 MHz NMR

Solid state NMR under ultra high field opens up new possibilities of experiments respect to spectral resolution and sensitivity of spectra. Unfortunately, none of sample temperature controllable solid-state NMR probes are available in ultra high field NMR facilities in Japan. This situation restricts usability and possibilities of solid state NMR studies under ultra high field in Japan.

In order to overcome this situation, we have developed  $^1\text{H}$ - $^{13}\text{C}$  double resonance VT-MAS probe based on JEOL 920MHz MAS probe. We have designed original VT control system for MAS probe, machined parts and built in JEOL 920 MHz MAS probe as show in Figure 1 (a). In the developed probe, a bearing gas for MAS was temperature controlled. Thus, all of bearing gas line was replaced by originally designed glass Dewar tubes. Since probe length was extremely long, Dewar was separated into two pieces. Those were jointed by optimally designed adapter, then a cartridge heater was built in bottom Dewar. The control of sample temperature was realized through feedback control of cartridge heater by monitoring gas temperature at a position close to sample tube. Upper and lower limits of available temperatures are limited by the material of stator and available chiller temperature, respectively. Stably available temperature range was verified experimentally from 0 to 60 °C which is sufficient range for studies of biomolecules.

Figure 1 (b) and (c) are photos of VT-MAS probe built in ultra high field magnet together with peripherals. For studies of biomolecules, precise temperature control of samples are required in order to retain those structures and functions. It is expected that this probe opens up the possibilities of studies for such samples. Finally the author K.N. appreciates to members of Equipment Development Center in IMS for their help.



**Figure 1.** (a) The bottom view of newly developed VT-MAS probe. (b) The side view of VT-MAS probe loaded into 920 MHz ultra high field magnet (21.6 T). (c) The side view of VT-MAS probe and peripherals enabling VT.

## 2. Structural Characterization of Peripheral Membrane Protein by Solution and Solid State NMR

Phospholipase C- $\delta$ 1 (PLC- $\delta$ 1) hydrolyzes phosphatidylinositol 4,5-bisphosphate (PIP<sub>2</sub>) in the plasma membrane to produce the second messengers on the membrane surface. The pleckstrin homology (PH) domain in the N-terminus of PLC- $\delta$ 1 selectively forms high affinity complex with PIP<sub>2</sub> in the plasma membrane and inositol 1,4,5-triphosphate (IP<sub>3</sub>) in the cytoplasm. Consequently those complex formations regulate

membrane localization of PLC- $\delta$ 1. So far, we have reported rat-PLC- $\delta$ 1 PH domain changes its conformation depending on curvatures of lipid bilayers and micelles.<sup>1)</sup> In this study, we established the over expression system of the PH domain of human PLC- $\delta$ 1, and performed preliminary NMR analysis of the recombinant protein.

The plasmid containing the hPH gene, corresponding to the PH domain (residues 1-142) of human PLC- $\delta$ 1, was transformed into *Escherichia coli* BL21(DE3) strain. To produce the isotope labeled hPH, the transformed *E. coli* was incubated in M9 medium containing stable isotopes. The harvested *E. coli* cells were purified using GST-affinity chromatography followed by gel-filtration chromatography. The purified hPH shows IP<sub>3</sub>-binding activity as judged by Native PAGE gel shift analysis (data not shown), indicating that the recombinant protein is correctly folded.

Figure 2 shows two-dimensional <sup>1</sup>H-<sup>15</sup>N heteronuclear single quantum coherence (HSQC) solution NMR spectra of the ligand-free (black signals) and IP<sub>3</sub>-complex forms (red signals) of the uniformly <sup>15</sup>N-labeled hPH. The chemical shift dispersion of the <sup>1</sup>H and <sup>15</sup>N resonances in the spectrum of the ligand-free hPH also indicated that the recombinant hPH is substantially folded. The addition of IP<sub>3</sub> resulted in chemical shift displacements of many resonances (Figure 2, red signals), indicating that the IP<sub>3</sub> binding induces a large conformational change of hPH. Solid state NMR studies of the hPH-PIP<sub>2</sub> complex in membrane, as well as ligand-binding studies for the several mutants of hPH, are in progress.

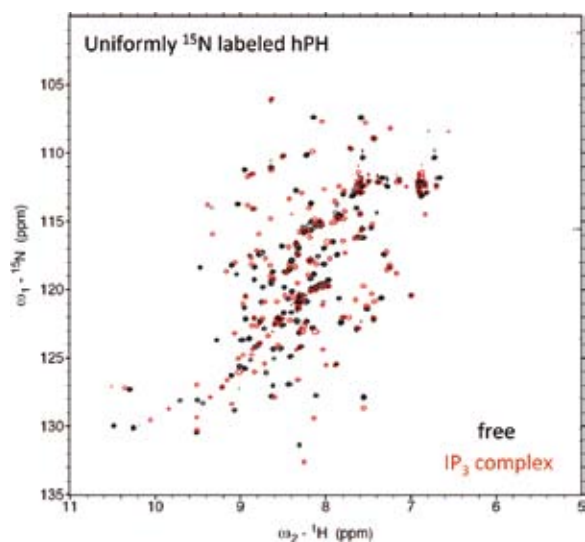


**Figure 2.** <sup>1</sup>H-<sup>15</sup>N HSQC solution NMR spectra of uniformly <sup>15</sup>N-labeled hPH in the absence (black) and the presence of IP<sub>3</sub> (red) at 20 °C. Molar ratio of hPH and IP<sub>3</sub> was 1:1.3.

### 3. <sup>2</sup>H QCPMG NMR of Paramagnetic Solids as a Probe of Molecular Dynamics

Solid state NMR is a powerful technique to investigate

dynamics of molecules and ions in substances. In particular, deuterium (<sup>2</sup>H,  $I = 1$ ) NMR can probe motions with timescale ranging from nanosecond to second by several methods such as a quadrupole echo, quadrupolar Carr-Purcell-Meiboom-Gill (QCPMG), magic-angle-spinning, two-dimensional NMR and relaxation experiments. Compared to measurement by the quadrupole echo sequence, the QCPMG technique where a train of spin echo generated by repeatedly irradiated refocusing pulses is acquired can enhance sensitivity of <sup>2</sup>H NMR spectra and extend dynamic range, although it has been employed only for diamagnetic compounds. Recently, we have developed a <sup>2</sup>H QCPMG method efficient for paramagnetic solids.

In this work, we applied the QCPMG method to probe molecular dynamics of paramagnetic solids. Figure 3 shows temperature dependences of <sup>2</sup>H NMR spectra of paramagnetic powder of CoSiF<sub>6</sub>·6H<sub>2</sub>O under 9.4 T. Asymmetric lineshape is caused by the paramagnetic interaction between <sup>2</sup>H and unpaired electrons in Co<sup>2+</sup>. For the QCPMG spectra, drastic change was observed in this temperature range, which is due to a reorientation of [Co(H<sub>2</sub>O)<sub>6</sub>]<sup>2+</sup> around the C<sub>3</sub> axis. For the echo spectra, however, lineshape of the spectra at low temperatures (293–313 K) are almost the same and small change was observed at high temperatures (373–393 K). By a simulation of the QCPMG spectra (Figure 3(ii)), <sup>2</sup>H interaction parameters of quadrupole coupling constant ( $C_Q$ ) and asymmetric parameter ( $\eta$ ) as well as a rate constant for the reorientational motion of [Co(H<sub>2</sub>O)<sub>6</sub>]<sup>2+</sup> ( $k_{re}$ ) also shown in the Figure 3 were obtained successfully. With these parameters, the echo spectra were reproduced (Figure 3(iv)). It was found that the <sup>2</sup>H QCPMG technique to extend dynamic range is also effective for paramagnetic compounds.

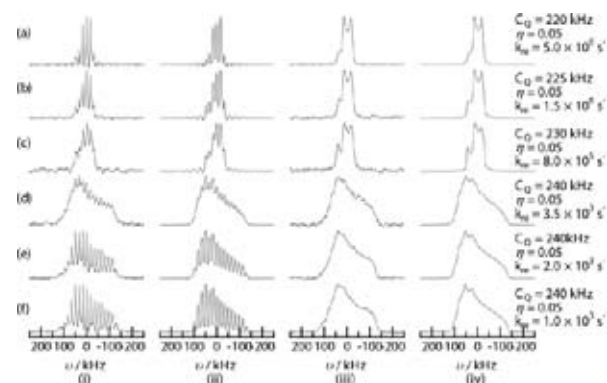


**Figure 3.** Temperature dependence of <sup>2</sup>H NMR spectra of paramagnetic CoSiF<sub>6</sub>·6H<sub>2</sub>O obtained by the QCPMG (i, ii) and echo (iii, iv) sequences. (i, iii) and (ii, iv) show the observed and simulated spectra, respectively. (a)–(f) are the spectra at 393, 383, 373, 313, 303 and 293 K, respectively.

#### Reference

- 1) N. Uekama, T. Aoki, T. Maruoka, S. Kurisu, A. Hatakeyama, S. Yamaguchi, M. Okada, H. Yagisawa, K. Nishimura and S. Tuzi, *Biochim. Biophys. Acta* **1788**, 2575–258 (2009).

# Organic Solar Cells

Research Center for Molecular Scale Nanoscience  
Division of Molecular Nanoscience



HIRAMOTO, Masahiro  
KAJI, Toshihiko  
IKETAKI, Kai  
NAKAO, Satoru  
SHINMURA, Yusuke  
KUBO, Masayuki  
YOKOYAMA, Kazuya  
YOSHIOKA, Tadashi  
ISHIYAMA, Norihiro  
OTSUBO, Yuko  
SUGIHARA, Hidemi

Professor  
Assistant Professor  
IMS Fellow  
Post-Doctoral Fellow  
Research Fellow  
Research Fellow  
Research Fellow  
Research Fellow  
Graduate Student  
Secretary  
Secretary

Organic solar cell is recognized as a future 3rd generation solar cell. In 2009, we started CREST Project; “Bandgap Science for Organic Solar Cells.” Target of this project is 15% efficiency of organic solar cells by establishing bandgap science for organic semiconductors, which is equivalent to that for silicon semiconductor.

Conductivity ( $\sigma$ ) is related both carrier concentration ( $n$ ) and carrier mobility ( $\mu$ ) [ $\sigma = en\mu$ ]. To achieve high efficiency, cell resistance ( $\rho = 1/\sigma$ ) should be decreased by increasing both  $n$  and  $\mu$ . Former and latter relate Topics 1, 2 and Topic 3, respectively.

## 1. Conduction-Type Control of $C_{60}$ Films from $n$ - to $p$ -Type by $MoO_3$ Doping<sup>1)</sup>

As in the case of inorganic solar cells, precise conduction type control, *i.e.*,  $pn$ -control is indispensable to fabricate efficient organic solar cells consisting of  $pn$  and  $pin$  junctions.

In this study, conduction-type control of highly purified 7N (seven nines; 99.99999%)  $C_{60}$  films from  $n$ - to  $p$ -type by doping with molybdenum oxide ( $MoO_3$ ) was demonstrated. The energetic value of the Fermi level ( $E_F$ ), 4.50 eV, for nondoped  $C_{60}$  films measured by the Kelvin vibrating capacitor method was positively shifted to 5.88 eV, and approached the valence band by the coevaporated doping of  $MoO_3$  at a

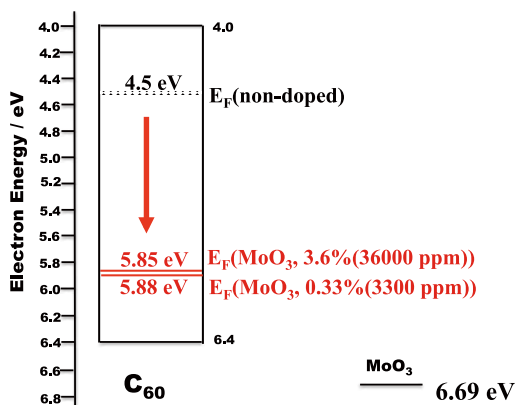


Figure 1. Positive shift of Fermi level ( $E_F$ ) for  $C_{60}$  films by  $MoO_3$  doping.

concentration of 3300 ppm (Figure 1).

Due to the observation of charge transfer (CT) absorption between  $C_{60}$  and  $MoO_3$ , and ability of electron extraction of  $MoO_3$  from the valence band of  $C_{60}$  (Figure 1), we concluded that the formation of CT complex [ $C_{60}^+-MoO_3^-$ ]. Positive charge on  $C_{60}^+$  can be liberated from the negative charge of the  $MoO_3^-$  by the heat energy of room temperature (Figure 2). Increase of the free hole concentration causes the large positive shift of  $E_F$ . Formation of  $p$ -type  $C_{60}$  was also confirmed based on the photovoltaic properties.

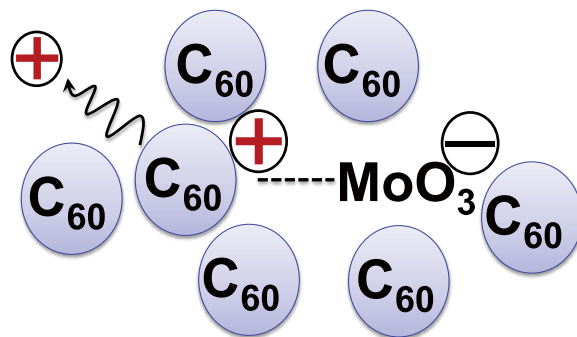


Figure 2. Mechanism of  $MoO_3$ -doping.

## 2. Doping-Based Control of the Energetic Structure of Photovoltaic Co-Deposited Films<sup>2)</sup>

Doping based  $pn$ -control technique for co-deposited films should be developed to enhance cell efficiency since recent organic solar cells incorporate co-deposited films to generate significant photocurrent densities based on the dissociation of excitons by the photoinduced electron transfer process.

In this study, energetic structures of  $C_{60}$ :6T ( $\alpha$ -sexithiophene) co-deposited films were intentionally tuned from  $n$ -type Schottky junctions through metal/intrinsic/metal junctions to  $p$ -type Schottky junctions by ppm-level doping with  $MoO_3$ .

‘Three component co-evaporation’ technique was developed for the doping of  $MoO_3$  into the  $C_{60}$ :6T co-deposited films. Precise monitoring of the deposition rate of the  $MoO_3$

using a computer monitoring system allowed us to dope with  $\text{MoO}_3$  to as low as 70 ppm in volume concentration. Light was irradiated on ITO electrode for the cells, ITO/ $\text{MoO}_3$ -doped  $\text{C}_{60}$ :6T/ $\text{MoO}_3$ /Ag (Figure 3).

For non-doped (0 ppm) and 400 ppm  $\text{MoO}_3$ -doped cells, photocurrent appeared in the region from 500 to 700 nm, where there is weak absorption from the cells (masking effect). This means that an *n*-type Schottky junction was formed at the  $\text{C}_{60}$ :6T/ $\text{MoO}_3$  interface (Figure 4(a)). For 600 ppm-doped cell (Figure 3), the photocurrent was distributed equally throughout the wavelength region from 300 to 700 nm, *i.e.*, the generation of photocurrent occurs in the whole of the bulk of the cell. This means that the co-deposited film behaves as 'intrinsic' material (Figure 4(b)). For 1100 and 4300 ppm-doped cells (Figure 3), photocurrent appeared in the strong absorption region (300–500 nm). This means that a *p*-type Schottky junction was formed at the ITO/ $\text{C}_{60}$ :6T interface (Figure 4(c)).

We are now trying to fabricate *pn*- and *pin*-homojunctions to create built-in potentials directly in the co-deposited films to realize high efficient organic solar cells.

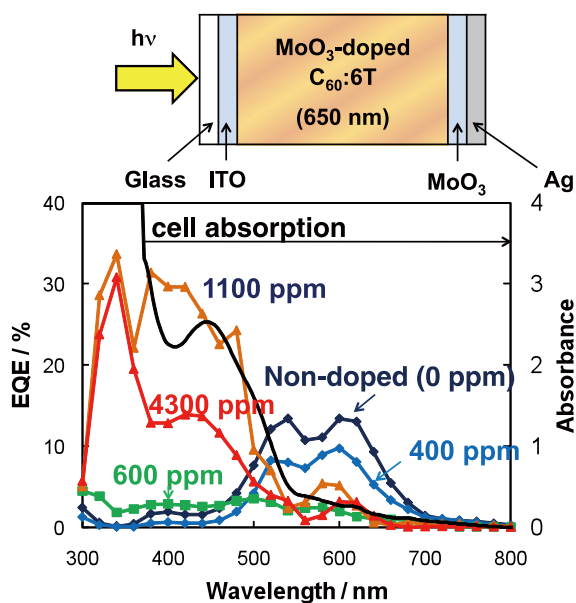


**Figure 3.** Action spectra of the external quantum efficiency (EQE) of the short-circuit photocurrent. Black curve shows cell absorption.

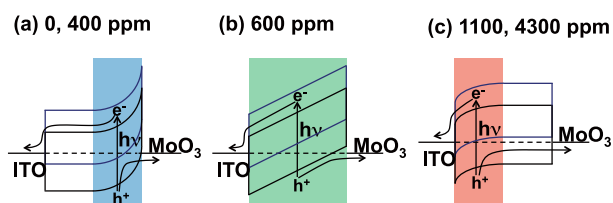


**Figure 4.** Energetic structures of the ITO/ $\text{C}_{60}$ :6T/ $\text{MoO}_3$  cells for various  $\text{MoO}_3$ -doping concentrations.

### 3. Co-Evaporant Induced Crystalline Co-Deposited Films in Organic Solar Cells<sup>3)</sup>

Nano-structure control of co-deposited films, *i.e.*, route formation for electrons and holes photogenerated in the co-deposited films is indispensable to fabricate efficient organic solar cells.

In this study, a novel method for crystallizing co-deposited films is developed. This method utilizes a liquid as a non-sticking co-evaporant during vacuum deposition (Figure 5).

Photocurrent enhancement was observed particularly for relatively thick (~400 nm) co-deposited films having greater light absorption (Figure 5). Co-deposited films based on  $\text{H}_2\text{Pc}$  and  $\text{C}_{60}$  with much improved crystallinity have been produced by introducing co-evaporant and confirmed by analysis using UV-Vis, XRD and FESEM (Figure 5). Striking enhancement in photocurrent generation is achieved in organic solar cells without exception, based on a variety of co-deposited films such as  $\text{PbPc}:\text{C}_{60}$ ,  $\text{AlClPc}:\text{C}_{60}$ , and  $\text{rubrene}:\text{C}_{60}$ . We believe that this method is generally applicable for growing high-quality crystalline films by vacuum deposition and opens the possibility of producing high-performance organic solar cells.

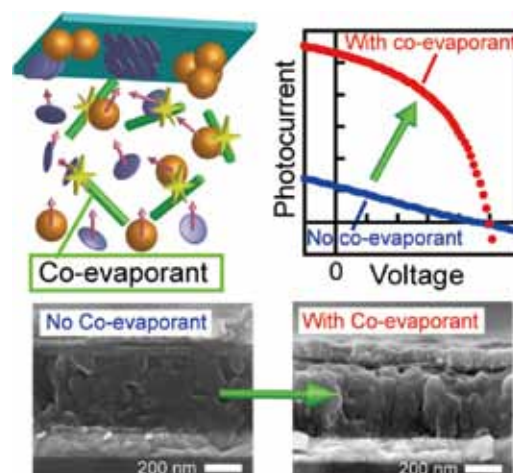


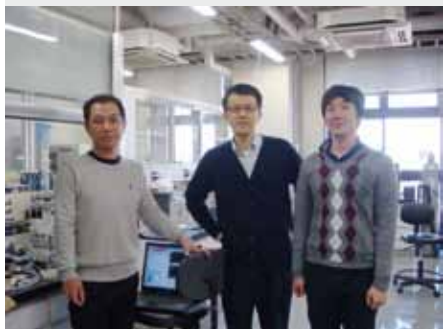
**Figure 5.** (Upper-left) Model of co-evaporant induced crystallization. Additional co-evaporant molecules hit  $\text{C}_{60}$  and phthalocyanines (Pc) at or near the substrate and promoting crystallization in the co-deposited film. (Upper-right) Photocurrent-voltage characteristics of  $\text{H}_2\text{Pc}:\text{C}_{60}$  co-deposited cells with/without co-evaporants, showing dramatic improvements of cell performances. (Lower) Enhanced crystallization is clearly observed in the co-deposited film with a co-evaporant, including a transformation of the grain from a random structure without the co-evaporant to a column structure with the co-evaporants.

#### References

- 1) M. Kubo, K. Iketaki, T. Kaji and M. Hiramoto, *Appl. Phys. Lett.* **98**, 073311 (2011).
- 2) N. Ishiyama, M. Kubo, T. Kaji and M. Hiramoto, *Appl. Phys. Lett.* **99**, 133301 (2011).
- 3) T. Kaji, M. Zhang, S. Nakao, K. Iketaki, K. Yokoyama, C. W. Tang and M. Hiramoto, *Adv. Mater.* **23**, 3320 (2011).

# Development of Organic Semiconductors for Molecular Thin-Film Devices

Research Center for Molecular Scale Nanoscience  
Division of Molecular Nanoscience



SUZUKI, Toshiyasu  
SAKAMOTO, Youichi  
KURODA, Yasuhiro  
WATANABE, Yoko

Associate Professor  
Assistant Professor  
Graduate Student  
Secretary

Organic light-emitting diodes (OLEDs) and organic field-effect transistors (OFETs) based on  $\pi$ -conjugated oligomers have been extensively studied as molecular thin-film devices. Organic semiconductors with low injection barriers and high mobilities are required for highly efficient OLEDs and OFETs. Radical cations or anions of an organic semiconductor have to be generated easily at the interface with an electrode (or a dielectric), and holes or electrons must move fast in the semiconducting layer. Compared with organic p-type semiconductors, organic n-type semiconductors for practical use are few and rather difficult to develop. Recently, we found that perfluorinated aromatic compounds are efficient n-type semiconductors for OLEDs and OFETs.

## 1. Selective and Random Syntheses of $[n]$ Cycloparaphenylenes ( $n = 8-13$ ) and Size Dependence of Their Electronic Properties<sup>1)</sup>

$[n]$ Cycloparaphenylenes ( $n = 8-13$ , CPPs) were synthesized, and their physical properties were systematically investigated. [8] and [12]CPPs were selectively prepared from the reaction of 4,4'-bis(trimethylstannyl)biphenyl and 4,4''-bis(trimethylstannyl)terphenyl, respectively, with Pt(cod)Cl<sub>2</sub> (cod = 1,5-cyclooctadiene) through square-shaped tetranuclear platinum intermediates. A mixture of [8]–[13]CPPs was prepared in good combined yields by mixing biphenyl and terphenyl precursors with platinum sources. Products were easily separated and purified by using gel permeation chromatography. In <sup>1</sup>H NMR spectra, the proton of the CPPs shifts to a lower field as  $n$  increased due to an anisotropic effect from the nearby PP moieties. Although the UV-vis spectra were rather insensitive to the size of the CPPs, the fluorescence spectra changed significantly in relation to their size. A larger Stokes shift was observed for the smaller CPPs. Redox properties of the CPPs were measured for the first time by using cyclic

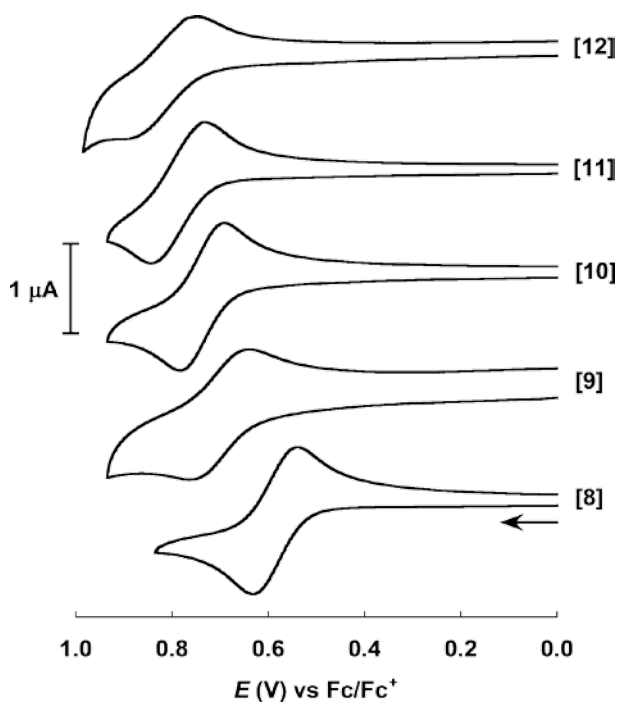


Figure 1. [8], [10], and [12]CPPs.

voltammetry, and the smaller CPPs had lower oxidation potentials. The results are consistent with the HOMO energies of CPPs, of which the smaller CPPs had higher energies.

#### Reference

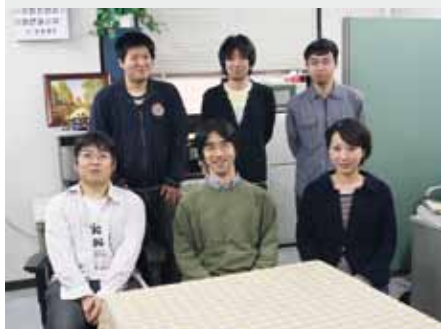
- 1) T. Iwamoto, Y. Watanabe, Y. Sakamoto, T. Suzuki and S. Yamago, *J. Am. Chem. Soc.* **133**, 8354–8361 (2011).



**Figure 2.** Cyclic voltammograms of [8] to [12]CPPs at 100 mV/s in 1,1,2,2-tetrachloroethane containing 0.1 M  $(n\text{-Bu})_4\text{NPF}_6$ .

# Building Photosynthesis by Artificial Molecules

Research Center for Molecular Scale Nanoscience  
Division of Molecular Nanoscience



NAGATA, Toshi  
KAWAO, Masahiro  
KON, Hiroki  
MIURA, Takahiro  
YUSA, Masaaki  
WANATABE, Yoko

Associate Professor  
IMS Fellow  
Post-Doctoral Fellow  
Graduate Student  
Graduate Student  
Secretary

The purpose of this project is to build nanomolecular machinery for photosynthesis by use of artificial molecules. The world's most successful molecular machinery for photosynthesis is that of green plants—the two photosystems and related protein complexes. These are composed almost exclusively from organic molecules, plus a small amount of metal elements playing important roles. Inspired by these natural systems, we are trying to build up multimolecular systems that are capable of light-to-chemical energy conversion. At present, our interest is mainly focused on constructing necessary molecular parts.

## 1. Photoreaction of Zinc Porphyrin/Co(II) Polypyridine Dyad Molecules with Hydroquinones as Electron Donors

Combination of photoinduced electron transfer and redox chemistry of transition metal complexes is an attractive way to achieve useful photochemical energy and materials conversion. We are particularly interested in systems having organic pigments as photosensitizers and first-row transition metals as catalytic sites.

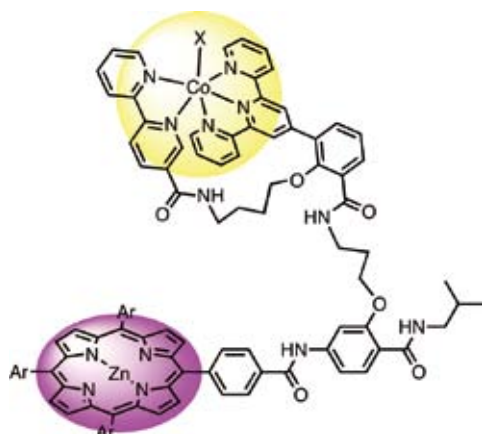


Figure 1. The Zn porphyrin/Co(II) complex dyad molecules.

Along this line, we prepared a series of dyad molecules consisting of zinc porphyrins and cobalt(II) complex (Figure 1). By use of this dyad molecule as a catalyst, we developed a new photoreaction, in which chloroform is reduced to lower chlorinated hydrocarbons with hydroquinone as the electron donor. Hydroquinone is used as the intermediate electron carrier in natural photosynthesis and other biochemical energy conversion systems, and the present system is a novel example of photosynthetic model that utilizes hydroquinone as the electron donor.

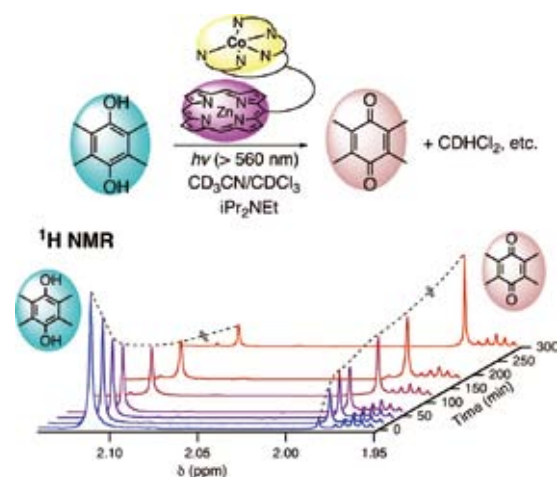


Figure 2. Photoreaction of ZnP/Co dyad with hydroquinone.

Although the detailed reaction mechanism of this photoreaction is still under investigation, one plausible mechanism is shown in Figure 3. The mechanism involves reductive quenching of the excited porphyrin by hydroquinone (or its anionic form), followed by charge shift reaction to generate the  $\text{Co}^{\text{I}}$  intermediate. The  $\text{Co}^{\text{I}}$  species is highly nucleophilic and will easily react with chlorocarbon to produce some active species, which eventually generates the product. This reaction should open the door to utilization of a regenerable electron donor in photochemical materials conversion.

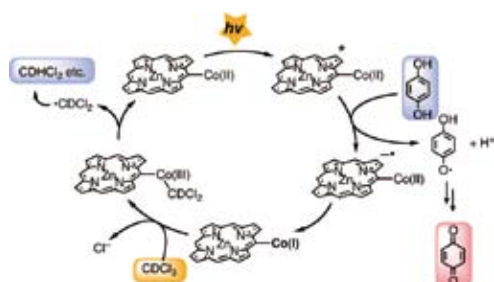


Figure 3. Plausible mechanism of the photoreaction.

## 2. Improved Synthesis of Single-Molecular Quinone Pools with Internal Redox Gradients and $^{19}\text{F}$ -NMR Handles

As demonstrated in the last section, hydroquinone/quinone interconversion is becoming important as a component of photochemical materials conversion. In this context, the “quinone pool” of natural photosynthesis should need much attention. The quinone pool in natural photosynthesis consists of a collection of plastoquinones embedded in thylacoid membranes, and transport electrons (and protons) between different redox enzymes.

Previously we reported our research on building “single-molecular” quinone pools by use of synthetic dendrimer molecules.<sup>1)</sup> Our next targets are (1) quinone pools containing two different quinones with different redox potentials, and (2) linearly extended quinone pools with two different photosystems on both ends. We synthesized the molecule shown in Figure 4, which is a third-generation dendrimer molecule with two different quinones in the internal positions. Although we had already published a quinone pool molecule based on a similar amide-dendrimer framework,<sup>2)</sup> our new synthesis employs introduction of protected quinones in the early stage of dendron synthesis, thus allowing generation-selective incorporation of different quinones.

## 3. Synthesis and Photoreaction of Soluble Phthalocyanines

Although porphyrins are very useful pigments in photo-synthetic model systems, they are not optimal in terms of utilizing solar light. In particular, they do not absorb light of wavelength longer than 650 nm, which limits usage of red to near-infrared light. Therefore, it is desirable to use pigments

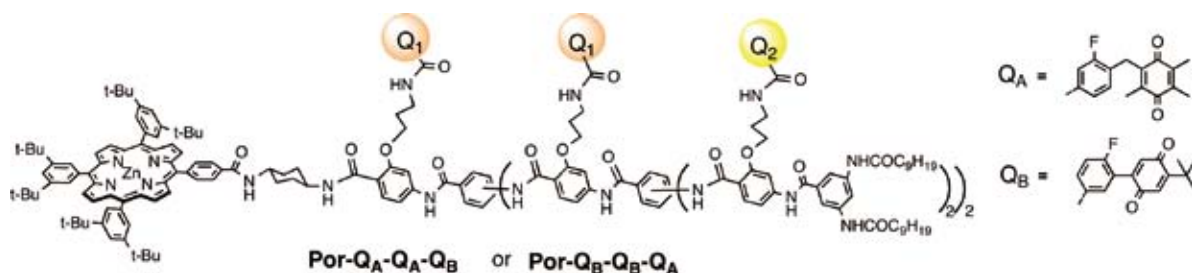


Figure 4. The third-generation quinone pool molecule with internal redox gradient.

that have strong absorption in this region. Phthalocyanines are good candidates as they have very strong absorption bands around 700 nm. However, incorporating phthalocyanines in complex molecular systems often causes difficulty because of the low solubility of phthalocyanine derivatives. To address this problem, we chose phthalocyanines having 2,4-di-tert-butylphenoxy substituents in the periphery. These phthalocyanines are very soluble in many organic solvents (including hexanes), so that the manipulation is easy.



Figure 5. Highly soluble phthalocyanines used in this work.

The high solubility of these phthalocyanines also allowed us to study photoreactions in a solution phase. Thus, the photoreduction of duroquinone by thiophenol was carried out in the presence of phthalocyanine and porphyrin. The results clearly show that phthalocyanine can utilize low-energy light more efficiently than porphyrin.

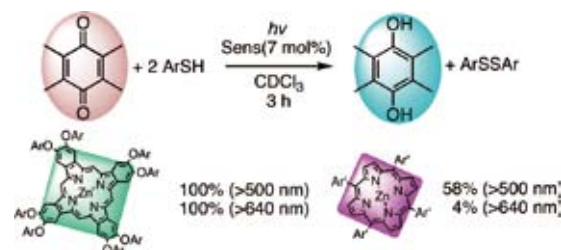


Figure 6. Comparison of photoreaction of phthalocyanine and porphyrin.

## References

- 1) T. Nagata and Y. Kikuzawa, *Biochim. Biophys. Acta* **1767**, 648–652 (2007).
- 2) T. Nagata, Y. Kikuzawa, T. Nagasawa and S. I. Allakhverdiev, *Trans. Mater. Res. Soc. Jpn.* **34**, 505–508 (2009).

# Chemistry of Bowl-Shaped Aromatic Compounds and Metal Nanocluster Catalysts

Research Center for Molecular Scale Nanoscience  
Division of Molecular Nanoscience



SAKURAI, Hidehiro  
HIGASHIBAYASHI, Shuhei  
TSURUOKA, Ryoji  
SAL PRIMA, Yudha S.  
MURUGADOSS, Arumugam  
TAN, Qi-Tao  
MORITA, Yuki  
KITAHARA, Hiroaki  
BAIG, Nasir R.  
GAYATRI, Gaddamanugu  
MISHRA, Vijaya Lakshmi  
KAEWMATI, Patcharin  
PONGPIPATT, Paweena  
HAESUWANNAKIJ, Setsiri  
ONOGI, Satoru  
DHITAL, Raghu Nath  
KATAOKA, Keita  
KARANJIT, Sangita  
SHRESTHA, Binod Babu  
PREEDASURIYACHAI, Patcharee  
NAKANO, Sachiko  
KAI, Noriko  
ISHIDA, Yuka  
KIM, Yukimi  
SASAKI, Tokiyo  
TANIWAKE, Mayuko

Associate Professor  
Assistant Professor  
IMS Fellow  
Visiting Scientist; JSPS Invited Fellow  
Visiting Scientist; JSPS Post-Doctoral Fellow  
Visiting Scientist; JSPS Post-Doctoral Fellow  
Post-Doctoral Fellow  
Post-Doctoral Fellow  
Post-Doctoral Fellow  
Visiting Scientist  
Visiting Scientist  
Visiting Scientist  
Visiting Scientist  
Visiting Scientist  
Graduate Student  
Graduate Student  
Graduate Student  
Graduate Student  
Graduate Student  
Graduate Student  
Graduate Student\*  
Technical Fellow  
Technical Fellow  
Technical Fellow  
Secretary  
Secretary

Bowl-shaped  $\pi$ -conjugated compounds including partial structures of the fullerenes, which are called “buckybowls,” are of importance not only as model compounds of fullerenes but also as their own chemical and physical properties. For example, in solution they show the characteristic dynamic behavior such as bowl-to-bowl inversion. On the other hand, they sometimes favor stacking structure in a concave-convex fashion in the solid state, giving excellent electron conductivity. Furthermore, some buckybowls are conceivable to possess the bowl-chirality if the racemization process, as equal as bowl-to-bowl inversion, is slow enough to be isolated. Very few buckybowls has been achieved for preparation mainly due to their strained structure, and no report on the preparation of chiral bowls has appeared. In this project, we develop the rational route to the various buckybowls with perfect chirality control using the organic synthesis approach.

We also investigate to develop novel catalytic properties of metal nanoclusters. We focus on the following projects: Preparation of size-selective gold nanoclusters supported by hydrophilic polymers and its application to aerobic oxidation catalysts: Synthetic application using metal nanocluster catalyst: Development of designer metal nanocluster catalyst using the highly-functionalized protective polymers.

## 1. The Impact of Basis Set Superposition Error on the Structure of $\pi$ - $\pi$ Dimers<sup>1)</sup>

The effect of basis set superposition error (BSSE) on the structure and energy of benzene, naphthalene, corannulene, and sumanene dimer has been analyzed. MP2 method was

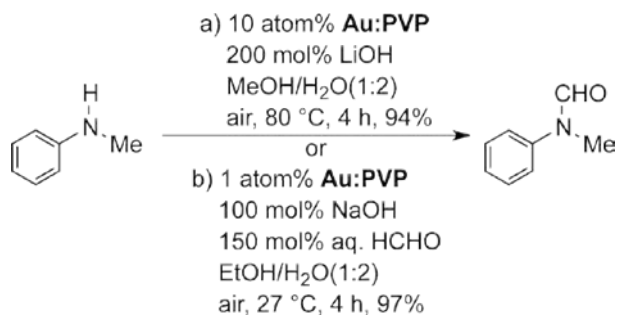
chosen and the effect is estimated using 6-31G, 6-31G(d), 6-311.G(d), cc-pVDZ, and cc-pVTZ basis sets. The model calculations on benzene dimer indicate that the impact of BSSE on the equilibrium geometry of  $\pi$ -stacked dimers appears to be quite significant. Calculations on larger molecular dimers such as the dimers of naphthalene, corannulene, and sumanene are also studied. Our results cautions that whenever a counterpoise correction is significant for the stacking interaction, it is essential to incorporate the BSSE in the geometry optimization. The most often adopted practice of including the BSSE only for the energy and not for the geometry may not be acceptable for stacking interactions. The impact of BSSE on structure and energy is much higher as the size of the monomeric units of stacked  $\pi$ -dimers is increased. The results on the stacking interactions of the two prototypical buckybowls, corannulene, and sumanene reveal that most of the pragmatic basis sets are essentially associated with a very high correction due to BSSE.

## 2. *N*-Formylation of Amines Catalyzed by Nanogold Under Aerobic Oxidation Conditions with MeOH or Formalin<sup>2)</sup>

Direct formation of amides from alcohols or aldehydes with amines has recently received attention from the viewpoint of the development of environmentally benign process. In particular, *N*-formylation of amines using MeOH or formaldehyde (especially formalin) is very important. The use of simple reactants makes it possible to understand the reaction mechanism. Furthermore, the starting materials are both

economical and the formamide derivatives produced in the reaction are important intermediates in organic synthesis. Until now, though, only a few examples of this transformation have been reported. Cu hydroxyl salts have been used in the presence of hydrogen peroxide. However, aerobic oxidation has been achieved with nanosize-gold supported on metal oxide with MeOH, and formylation of dimethylamine with formaldehyde has been carried out using metallic gold or silver surfaces as a catalyst. Practical procedures for *N*-formylation by aerobic oxidation that tolerate a wide scope of amines are still needed.

Nanosized-gold metal has recently attracted a great deal of interest because of its high activity and potential application in the emerging area of green oxidation chemistry. We have recently demonstrated that gold nanoclusters stabilized by poly(*N*-vinyl-2-pyrrolidone) (**Au:PVP**) act as an excellent quasi-homogenous catalyst for the aerobic oxidation of benzylic alcohols, generation of H<sub>2</sub>O<sub>2</sub> in the presence of ammonium formate, homo-coupling reaction of arylboronic acids, and other cyclization reactions. **Au:PVP** was found to be an excellent catalyst for the direct *N*-formylation of amine with MeOH or formalin as a formyl source. In particular, only 1 atom% of catalyst was needed and the reaction proceeded under ambient conditions in the reaction with formalin solution. The results strongly indicate that **Au:PVP** might possess superior catalytic activity toward the oxidation of hemiaminal intermediate when compared to other catalysts. Such characteristic features of **Au:PVP** will be applicable to many types of practical organic syntheses. We wish to report highly selective direct *N*-formylation using MeOH or formalin as a formyl source in the presence of **Au:PVP** under aerobic conditions.



### 3. Chitosan-Stabilized Gold, Gold–Palladium, and Gold–Platinum Nanoclusters as Efficient Catalysts for Aerobic Oxidation of Alcohols<sup>3)</sup>

Chitosan was used as a stabilizer for the synthesis of Au, AuPd and AuPt nanoclusters (NCs). The produced NCs had a narrow particle size distribution with sizes less than 2.3 nm in diameter and were characterized by various techniques such as

UV-Visible spectroscopy, X-ray diffraction, X-ray photoelectron spectroscopy, transmission electron microscopy and scanning electron microscope energy dispersive spectroscopy (STEM-EDS). These metal NCs exhibited high catalytic activity toward the aerobic oxidation of various alcohols under ambient conditions comparable with the reported **Au:PVP** catalyst. Au NCs protected by chitosan could easily be recovered for repeated use.

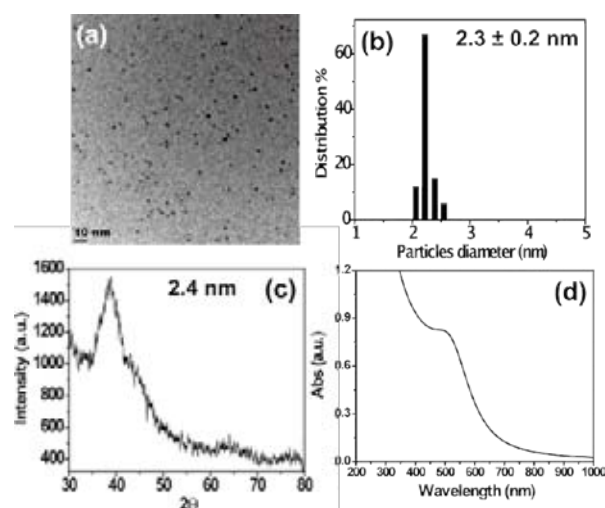


**Figure 1.** (a) TEM image of chitosan-stabilized Au NCs. (b) Particle size histogram plot obtained from (a). (c) X-ray diffraction pattern of Au:Chit. (d) UV-Visible spectrum of Au:Chit.

### 4. Magnetically Recoverable Magnetite/Gold Catalyst Stabilized by Poly(*N*-vinyl-2-pyrrolidone) for Aerobic Oxidation of Alcohols<sup>4)</sup>

Fe<sub>3</sub>O<sub>4</sub>:PVP/Au nanocomposite synthesized *via* a two-step procedure was tested as quasi-homogenous catalysts in alcohol oxidation. It was found that the nanocomposite was able to carry out aerobic oxidation of alcohols in water at room temperature. Studies show rapid magnetic recoverability and reusability characteristics.

#### References

- 1) D. Vijay, H. Sakurai and G. N. Sastry, *Int. J. Quantum Chem.* **111**, 1893–1901 (2011).
- 2) P. Preedasuriyachai, H. Kitahara, W. Chavasiri and H. Sakurai, *Chem. Lett.* **39**, 1174–1176 (2010).
- 3) A. Murugadoss and H. Sakurai, *J. Mol. Catal. A: Chem.* **341**, 1–6 (2011).
- 4) H. W. Chen, A. Murugadoss, T. S. A. Hor and H. Sakurai, *Molecules* **16**, 149–161 (2011).

\* carrying out graduate research on Cooperative Education Program of IMS with Chulalongkorn University

# Multifunction Integrated Macromolecules for Molecular-Scale Electronics

Research Center for Molecular Scale Nanoscience  
Division of Molecular Nanoscience



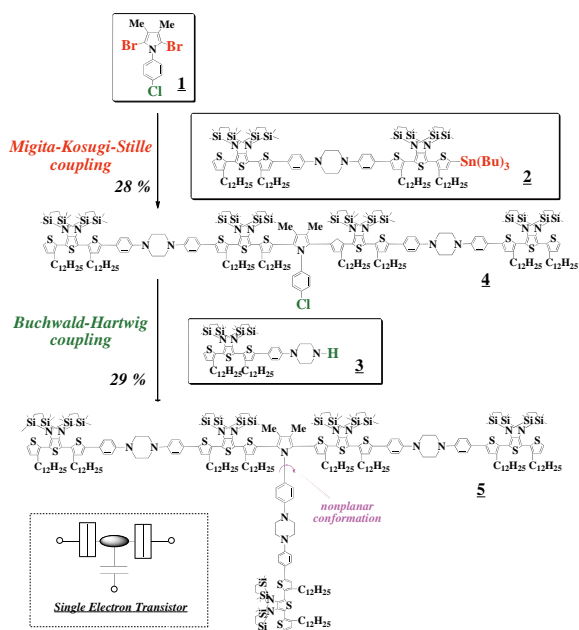
TANAKA, Shoji

Assistant Professor

Recently a single electron tunnel (SET) device has attracted much attention due to the growing demand for ultra-low-power device. A SET device manipulates an electron by means of one-by-one electron transfer, resulting in ultimately low power consumption. However, for room temperature operation, the size of SET device must be as small as a few nm to overcome the thermal fluctuation problems. The process size of a few nm is out of the range of conventional micro-technology. In this project, to establish an innovative fabrication process for SET device systems, we have been developing step-wise synthetic protocols for molecule-based single-electron tunnel devices (MOSET) and circuit.

## 1. Molecular Design for Mono-Molecular Integration of Basic Components of Single-Electron Devices

Single electron devices comprise three key elements: Coulomb island, tunnel junction, and capacitive junction. To integrate these elements in a single molecule, we have designed versatile molecular building blocks (1-3). Using these building blocks, we have synthesized the first trial model of a “mono-molecular” single-electron transistor (Scheme 1). Although there are a lot of issues to be solved, this is the first step to realize the practical MOSET device systems based on mono-molecular integration strategy.



Scheme 1. Step-wise Synthetic Route to Single-electron Transistor.

## 2. Mechanism of Electrical Conduction through Single Oligothiophene Molecules<sup>1)</sup>

The temperature dependence of electrical conductance of oligothiophene molecules with the length of 2.2 nm (5-mer), 5.6 nm (14-mer) and 6.7 nm (17-mer) was measured by break junction method with a scanning tunneling microscope to clarify the charge transport mechanisms. The conductance of 17-mer molecule increased exponentially with temperature whereas the conductance of 5-mer and 14-mer molecules did not change. These results indicate that the dominant charge transport mechanism changed from tunneling to thermally activated hopping at molecular length around 6.7 nm (17-mer).

### Reference

- 1) SK. Lee, R. Yamada, H. Kumazawa, H. Tada and S. Tanaka, *Funct. Mater. Lett.* **3**, 245–248 (2010).

# Development of Novel Heterocyclic Compounds and Their Molecular Assemblies for Advanced Materials

## Safety Office



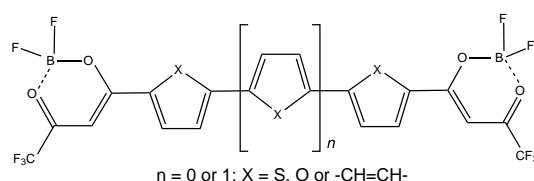
TOMURA, Masaaki

Assistant Professor

Heterocycles containing sulfur and/or nitrogen atoms are useful as components of functional organic materials since heteroatoms in their rings are helpful to stabilize ions or ion-radical species. In addition, intermolecular interactions caused by heteroatom contacts can be expected to form unique molecular assemblies. In this project, novel functional organic materials based on various heterocycles were synthesized and their physical and structural properties were investigated.

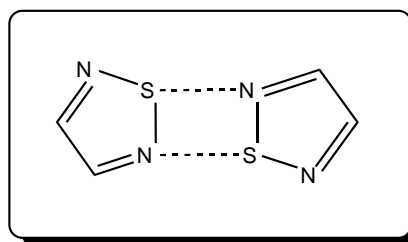
## 1. Synthesis and Properties of Terthiophene and Bithiophene Functionalized by $\text{BF}_2$ Chelation: A New Type of Electron Acceptor Based on Quadrupolar Structure<sup>1)</sup>

Terthiophene and bithiophene derivatives functionalized by  $\text{BF}_2$  chelation were synthesized as a new type of electron acceptor, and their properties were compared to those of bifuran and biphenyl derivatives. These new compounds are characterized by quadrupolar structures due to resonance contributors generated by  $\text{BF}_2$  chelation. The bithiophene derivative has a strong quadrupolar character compared with the bifuran and biphenyl derivatives because their hydrolytic analyses indicated that the bithiophene moiety has a larger on-site Coulomb repulsion than the others. The terthiophene derivative has a smaller on-site Coulomb repulsion than the bithiophene derivative due to the addition of a thiophene spacer. These  $\text{BF}_2$  complexes exhibit long-wavelength absorptions and according to measurements of ionization potentials and absorption edges they have energetically low-lying HOMOs and LUMOs. The crystal structure of the bithiophene derivative is of the herringbone type, with short  $\text{F}\cdots\text{S}$  and  $\text{F}\cdots\text{C}$  contacts affording dense crystal packing. n-Type semiconducting behavior was observed in organic field-effect transistors based on these  $\text{BF}_2$  complexes.



## 2. Theoretical Study of Intermolecular $\text{S}\cdots\text{N}$ Interactions in a 1,2,5-Thiadiazole Dimer

Ab initio (HF, MP2) and DFT (B3LYP, PW91PW91) calculations with the 6-31++G(2d,2p) basis sets have been performed on a 1,2,5-thiadiazole dimer. The binding energy of the dimer by MP2 corrected BSSE and ZPE is 3.37 kcal/mol, which is comparable to those of noncovalent  $\text{C-H}\cdots\text{O}$  and  $\text{C-H}\cdots\pi$  interactions. The HF and DFT method extremely underestimated the binding energies as compared to MP2. This fact indicates that the dispersion interaction is significantly important for the intermolecular  $\text{S}\cdots\text{N}$  interaction in the dimer. The optimized  $\text{S}\cdots\text{N}$  distance (3.022 Å) by MP2 is in good agreement with crystallographic data.



## Reference

- 1) K. Ono, A. Nakashima, Y. Tsuji, T. Kinoshita, M. Tomura, J. Nishida and Y. Yamashita, *Chem. -Eur. J.* **16**, 13539–13546 (2010).

## Visiting Professors



Visiting Professor  
**OHTA, Nobuhiro** (from *Hokkaido University*)

### Photoirradiation Effects on Structure, Dynamics and Material Properties

Photoinduced change in electrical conductivity as well as in structure and dynamics has been examined for various materials with the time-resolved measurements of resistance and/or luminescence following photoirradiation. In the photoirradiated organic crystals, conductivity switching and bistability of current over certain ranges of applied voltages have been observed. In organic superconductors, photoinduced change in the electrical conductivity has also been examined at temperatures in the vicinity of the metal–superconductor (M–S) phase transition temperature, and unconventional asymmetry of critical slowing down about the M–S transition temperature has been found. In ionic conductor such as silver iodide, photoirradiation effect on ionic conductivity has been observed, depending on the excitation wavelength. To understand the photoirradiation effect as well as the synergy effect of photoirradiation and applied electric field on electrical conductivity, photoirradiation effects not only on the electrical conductivity but also on the magnetic property will be examined.



Visiting Professor  
**ABE, Manabu** (from *Hiroshima University*)

### Singlet Biradical Chemistry: $\pi$ -Single Bonded Species

Localized singlet biradicals have been recognized as putative intermediates in processes involving homolytic bond-cleavages and formations. To understand the homolytic reactions, the singlet biradicals should be detected at least using conventional spectroscopic analyses. To this end, we needed to design and generate relatively long-lived singlet biradicals, in which the singlet state should be the ground state spin-multiplicity. In cyclopentane-1,3-diyl systems, we have found the notable substituent effect on lowering the singlet state energetically than the triplet state. Thus, the 2,2-dialkoxycyclopentane-1,3-diyls were calculated to be the singlet ground state molecules. The 1,3-diphenyl substitution of the 1,3-biradicals allowed us to detect experimentally the singlet biradical at nano-second time scale. The species was found to be observed at  $\lambda_{\text{max}}$  600 nm, which is persistent below the temperature of liquid nitrogen. The electronic transition was calculated to be corresponding to the  $\pi \rightarrow \pi^*$  transition, which means that the singlet species possess a character of  $\pi$ -single bond.



Visiting Professor  
**KATO, Tatsuhisa** (from *Kyoto University*)

### Studies of Molecular Magnetization of Super-Molecules Relating Fullerenes

People distinguish electrons in terms of Cartesian coordinates in space as well as of spin ones. Although both coordinates are independent, some spin states are specified by the electron configuration on the levels of electronic wave function in space because of anti-symmetry with exchange of electrons. In this manner the electronic structure of molecules can be characterized through the measurement of spins. The high-spin states of metallo-fullerenes and molecular complexes were investigated by high-field and pulsed electron spin resonance (ESR) spectrometers. For example, the dimetallic endohedral heterofullerene,  $\text{Gd}_2@C_{79}\text{N}$ , was characterized by a half-integer spin quantum number of  $S = 15/2$  by ESR measurements. The result described an exceptionally stable paramagnetic molecule with low chemical reactivity, whose unpaired electron spins were localized on the internal diatomic gadolinium cluster.